Title

Full-wavefield inversion of surface waves for mapping embedded low-velocity zones in permafrostSurface-wave inversion for permafrost

Journal

Geophysics, 79(6)

ISSN

0016-8033

Authors

Dou, Shan
Ajo-Franklin, Jonathan B

Publication Date

2014-11-01

DOI

10.1190/geo2013-0427.1

Peer reviewed

Full-wavefield inversion of surface waves for mapping embedded low-velocity zones in permafrost

Article History

Received: 15 November 2013
Accepted: 29 July 2014
Published: 23 September 2014

Publication Data

ISSN (print): 0016-8033
ISSN (online): 1942-2156
CODEN: GEO

Keywords

permafrost, surface wave, near surface, inversion, shear wave (S-wave)

Shan Dou[1] **and Jonathan B. Ajo-Franklin**[2]

[1]**University of California, Berkeley, Department of Earth and Planetary Science, Berkeley, California, USA. E-mail: shandou@berkeley.edu**

[2]**Lawrence Berkeley National Laboratory, Earth Sciences Division, Berkeley, California, USA. E-mail: jbajo-franklin@lbl.gov**

Sections: ChooseAbstractINTRODUCTIONBACKGROUNDMETHODSSYNTHETIC TESTSFIELD DATA INVERSIONDISCUSSIONCONCLUSION ACKNOWLEDGMENTSREFERENCESAPPENDIX APARAMETER SETTI...APPENDIX BEMPIRICAL EQUAT...CITING ARTICLES

Choose Top of pageAbstract <<INTRODUCTIONBACKGROUNDMETHODSSYNTHETIC TESTSFIELD DATA INVERSIONDISCUSSIONCONCLUSIONACKNOWLEDGMENTSREFERENCESAPPENDIX APARAMETER SETTI...APPENDIX BEMPIRICAL EQUAT...CITING ARTICLES

Abstract

Surface waves are advantageous for mapping seismic structures of permafrost, in which irregular velocity gradients are common and thus the effectiveness of refraction methods are limited. Nevertheless, the complex velocity structures that are common in permafrost environments often yield unusual dispersion spectra, in which higher-order and leaky modes are dominant. Such unusual dispersion spectra were prevalent in the multichannel surface-wave data acquired from our permafrost study site at Barrow, Alaska. Owing to the difficulties in picking and identifying dispersion curves from these dispersion spectra, conventional surface-wave inversion methods become problematic to apply. To overcome these difficulties, we adopted a full-wavefield method to invert for velocity models that can best fit the dispersion spectra instead of the dispersion curves. The inferred velocity models were consistent with collocated electric resistivity results and with subsequent confirmation cores, which indicated the reliability of the recovered seismic structures. The results revealed embedded low-velocity zones underlying the ice-rich permafrost at our study site — an unexpected feature considering the low ground temperatures of $-10°C$−10°C to $-8°C$−8°C. The low velocities in these zones ($\sim 70\%–80\%$~70%–80% lower than the overlying ice-rich permafrost) were most likely caused by saline pore-waters that prevent the ground from freezing, and the resultant velocity structures

are vivid examples of complex subsurface properties in permafrost terrain. We determined that full-wavefield inversion of surface waves, although carrying higher computational costs than conventional methods, can be an effective tool for delineating the seismic structures of permafrost.

Permalink: https://doi.org/10.1190/geo2013-0427.1
Keywords: permafrost, surface wave, near surface, inversion, shear wave (S-wave)

Choose Top of pageAbstractINTRODUCTION <<BACKGROUNDMETHODSSYNTHETIC TESTSFIELD DATA INVERSIONDISCUSSIONCONCLUSIONACKNOWLEDGMENTSREFERENCESAPPENDIX APARAMETER SETTI...APPENDIX BEMPIRICAL EQUAT...CITING ARTICLES

INTRODUCTION

Permafrost — defined as frozen ground that stays at or below 0°C for at least two consecutive years — comprises 24% of the land in the northern circumpolar region (Jones et al., 2009). This vast permafrost-covered area houses approximately 50% of the terrestrial soil carbon pool (Zimov et al., 2006) and about 13% of the world's undiscovered, technically recoverable, oil resource (Gautier et al., 2009). Knowledge of permafrost properties is thus essential for ecosystem sustainability and future resource development. Nevertheless, permafrost is particularly difficult to study because it is largely invisible from the ground surface. Boreholes, although effective for subsurface characterization, are expensive and invasive and they are intrinsically point measurements. In contrast, geophysical approaches are cost-effective, mostly nonintrusive, and capable of resolving subsurface features at scales of tens to hundreds of meters laterally and vertically. Naturally, geophysical methods have been widely used to infer permafrost structures across various scales (see the review by Kneisel et al., 2008).

Among the available geophysical approaches, seismic techniques have been used in a variety of studies for permafrost characterizations (e.g., Justice and Zuba, 1986; Miller et al., 2000; Hauck and Kneisel, 2008; Hilbich, 2010; Ramachandran et al., 2011). Such research efforts are in especially high demand for seismic exploration in the Arctic regions: Because permafrost is a near-surface structure that often overlays deeper oil-bearing strata, its presence can complicate processing and interpretation by generating severe traveltime distortions. Knowledge of permafrost structures is therefore essential for applying static corrections (e.g., Cox et al., 1999; Strobbia et al., 2009; Trupp et al., 2009). However, despite widespread interest, permafrost remains a challenging target for seismic investigations. Seismic delineation of permafrost structures might seem trivial at first glance, given the marked velocity contrast between frozen and unfrozen ground (e.g., Timur, 1968; Zimmerman and King, 1986). The challenges, however, come from the fact that seismic velocities in permafrost are primarily controlled by ground-ice content rather than lithology. In near-surface structures that are mainly controlled by lithology, it is often sufficient to assume a "layer-cake" earth model comprised of dry surface soil, wet overburden, weathered bedrock, and fresh bedrock. In this case, seismic velocities increase with depth, and thus commonly used seismic prospecting methods (e.g., refraction, reflection) are straightforward to apply. In contrast, although lithology does exert its influences, other factors such as thermal, chemical, and hydrological conditions can cause dramatic variations in ice/water content of permafrost; irregular distributions of ice and water in turn lead to complex seismic structures in permafrost. Because simple layering and monotonically increasing velocities with depth seldom exist within permafrost, body waves (P- and S-waves) that travel through the body of the medium usually are "blind" to embedded low-velocity features. Therefore, commonly used seismic prospecting methods based upon refraction analysis are often unable to provide reliable information about permafrost structures (e.g., Barnes, 1963; Trupp et al., 2009).

In contrast, surface-wave methods do not require abrupt velocity contrasts or normal velocity gradients (increasing velocities with depth), and thus they can be used for mapping irregular velocity structures in permafrost. Furthermore, collecting high signal-to-noise ratio (S/N) surface-wave data usually is straightforward by using the same acquisition systems as those for refraction and reflection methods. Motivated by the development of the multichannel analysis of surface waves technique (Park et al., 1999; Xia et al., 1999), surface-wave methods have become widely accepted for applications in near-surface velocity characterizations (see the review by Socco et al., 2010). In particular, recent studies have shown the potential of applying such methods to the Arctic regions (Strobbia et al., 2009; Ke et al., 2010).

Although surface-wave methods are a viable option for seismic mapping of permafrost structures, distinct challenges also exist. For instance, in areas with thin permafrost, the near-surface material resembles a velocity model with a fast top layer (Ke et al., 2010); in areas with thick permafrost, layers or zones of unfrozen ground could occur as low-velocity layers or pockets that are enclosed in a high-velocity background (Strobbia et al., 2009; Trupp et al., 2009). The irregular velocity variations in permafrost, combined with the marked velocity contrasts between frozen and unfrozen materials, could render conventional surface-wave inversion methods inapplicable.

In this study, to investigate subsurface properties of permafrost, we applied dispersion analysis of surface waves to active-source seismic data sets collected along a series of off-end linear arrays at a site in the Arctic Coastal Plain near Barrow, Alaska. The surface-wave data exhibit inversely dispersive trends (i.e., phase velocities increase with increasing frequencies), for which conventional surface-wave inversion methods are inapplicable. As an alternative, we used a full-wavefield method equipped with a global-local hybrid optimization technique to infer the velocity

structure. Inversion results reveal the presence of pronounced low-velocity zones with S-wave velocities in the 300–680m/s300–680 m/s range — 70%–80% lower than the shallower permafrost units. The spatial extent of these low-velocity zones is also largely consistent with previously observed low electric resistivity features. These results suggest the possible existence of saline zones within permafrost that are unfrozen or only partially frozen due to the freezing-point depression effect of dissolved salts. This is a vivid example of the complex conditions in permafrost-affected ground, and the full-wavefield inversion of surface waves is an effective approach for quantitative delineation of permafrost.

BACKGROUND

Choose Top of pageAbstractINTRODUCTIONBACKGROUND <<METHODSSYNTHETIC TESTSFIELD DATA INVERSIONDISCUSSIONCONCLUSIONACKNOWLEDGMENTSREFERENCESAPPENDIX APARAMETER SETTI...APPENDIX BEMPIRICAL EQUAT...CITING ARTICLES

Field site description and data acquisition

Geologic setting of the field site

The Barrow peninsula (70.9° N–71.5° N, 155.4° W–157.5° W) is located at the northern extremity of the Arctic Coastal Plain in Alaska. Bounded by the Chukchi and Beaufort Seas of the Arctic Ocean, this triangular-shaped land mass is approximately 530-km north of the Arctic Circle, which yields a polar climate with mean annual air temperatures as low as −12°C−12°C. The entire area is underlain by continuous permafrost to depths of more than 300 m (Jorgenson et al., 2008), whereas the active layer (the topmost layer of soils that freeze and thaw seasonally) only reaches a thickness ranging from 30 cm to 90 cm (Hinkel and Nelson, 2003). Soil cores from Barrow indicate that the upper permafrost is ice-rich, with volumetric ice content averaging 50%–75% in the upper 2 m (Sellmann et al., 1975). The parent materials of the soils are unconsolidated Quaternary sediments of Gubik Formation that consist largely of silt, fine-grained sand, and a small amount of clay and gravel (Black, 1964; Williams and Carter, 1984). The sediments are primarily of marine origin, resulting from repeated regression and transgression of the Arctic Ocean (Thurston et al., 1987). The top of the bedrock is commonly found in boreholes at depths of about 10–30-m below the land surface (Collins and Brewer, 1961).

Active multichannel surface-wave survey

Our study area is within the Barrow Environmental Observatory (BEO), a research reserve consisting of 7466 acres of arctic tundra (Figure 1). As part of the Next-Generation Ecosystem Experiments project (NGEE-Arctic) initiated by the U.S. Department of Energy (DOE), we conducted a combined seismic refraction and surface-wave survey at the BEO site in May 2012. During the time of data acquisition, the air temperature remained below freezing and the active layer was completely frozen. We laid out 48 10-Hz vertical geophones in a linear array with 1.1-m receiver interval. Seismic data were acquired in a roll-along manner along a 475-m southeast–northwest-trending survey line using a 14-kg (30-lb) vertical sledgehammer source.

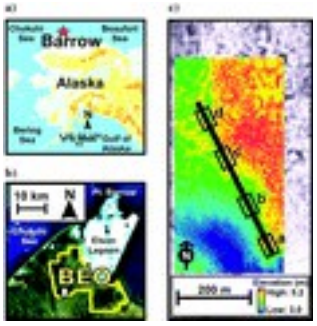

View larger version (138K)

Figure 1. Maps of the study area near Barrow, Alaska: (a) the Barrow area within Alaska (red star). (b) The location of the BEO (yellow outline). The gray box indicates the NGEE-Arctic geophysics study site. (c) The 475-m-long seismic survey line (the black southeast–northwest trending line). The colored background is a LiDAR measurement of the surface topography. The black boxes (a-d) denote the spatial locations that our study focuses on.

Note that with the vertical source and the vertical receivers, the type of surface waves we acquired are Rayleigh waves — a subset of surface-wave types. However, because most of the literature on near-surface geophysics uses *surface wave* rather than *Rayleigh wave*, we use surface wave throughout this paper.

Representative synthetic examples of surface-wave dispersion

Prior to the field data analysis, we consider a few synthetic examples that represent typical surface-wave dispersion patterns for near-surface (top 50–100 m) seismic investigations. As illustrated in Figure 2, model 1 (Figure 2a), in which S-wave velocity monotonically increases with depth, represents a normally dispersive medium; model 2 (Figure 2c) and 3 (Figure 2e), in which the S-wave velocities do not monotonically increase with depth (i.e., velocity reversals are present), represent irregularly dispersive media. Between the two irregularly dispersive media, model 2 has an embedded low-velocity layer and the highest velocity exists in its half-space, whereas model 3 has the highest velocity in its topmost layer.

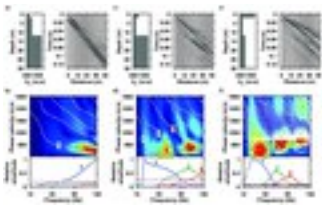

View larger version (66K)

Figure 2. Three representative layered velocity models and the corresponding synthetic wavefields: (a and b) Model 1, normally dispersive model, (c and d) model 2, irregularly dispersive model with an embedded low-velocity layer, (e and f) model 3, irregularly dispersive model with a high-velocity top layer. In (a, c, and e), the panel on the left shows the velocity structure of the model; the panel on the right shows the associated synthetic waveforms. In (b, d, and f), the pseudocolor image shows the dispersion spectrum. The superimposed white lines are the corresponding theoretical modal curves, and the colored lines are these modes' relative amplitudes (i.e., surface displacement distributions). A threshold in relative amplitudes for each velocity model is labeled by a magenta dashed line, denoting the threshold above which the mode amplitudes are strong enough to be present as spectral highlights. For each mode, the frequency range within which the relative amplitudes are above the threshold is denoted by open circles. The numeric labels 1, 2, and 3 denote the fundamental mode, the first overtone, the second overtone, and the third overtone, respectively.

The model structure and the dispersion behavior of surface waves are mathematically connected by the Rayleigh secular equation, which represents an eigenvalue problem derived from the equation of motion and the associated boundary conditions (no traction at the free surface and no traction and strain at infinite depth). Because a propagating surface wave train essentially is a superposition of its harmonic modes, the nontrivial eigenvalues of the Rayleigh secular equation are equivalent to the eigenfrequencies of the modes in space (wavenumber kk is the spatial frequency) and time (frequency ff is the temporal frequency). The phase velocity of each mode $v(f)$v(f) is obtained via $v(f)=2\pi f/k$v(f)=2πf/k, and the kinematic attributes of the wavefield carried by each mode can be expressed as a set of $(f,v$f,v) points called *modal curves*.

Although numerical modeling of modal curves can be achieved by searching for the nontrivial eigenvalues of the Rayleigh secular equation (i.e., the root-finding method), the measured modal curves (the dispersion curves) need to be extracted from dispersion spectra of the wavefield. The dispersion spectrum is generated by transforming the original wavefield in the offset-time (x-tx-t) domain into the frequency-velocity (f-vf-v) domain. It contains the complete signal content — comprised of kinematic and energy information — of the wavefield. For a normally dispersive medium, the dispersion spectrum usually has its energy concentrated along a smooth and continuous "ridge" (Figure 2b). This ridge corresponds to the fundamental mode that dominates the wavefield of the normally dispersive medium. A measured fundamental-mode dispersion curve can be extracted by picking the spectral maxima along the ridge, and its dispersion trend manifests that velocity decreases with frequency.

Although the fundamental mode dominates the wavefield of a normally dispersive medium, higher order modes can become equally or more energetic in irregularly dispersive media. To examine energy distribution among the modes for the representative examples, theoretical modal curves (calculated by the root-finding method implemented in Herrmann, 2004) are superimposed on the corresponding dispersion spectra and the associated amplitude

responses of individual modes are displayed underneath each dispersion spectrum (Figure 2b, 2d, and 2f). For model 1 (Figure 2b), the fundamental mode is predominant and different modal curves are distant from each other; the fundamental-mode energy form a continuous ridge. For model 2 (Figure 2d), at least three modes are strongly excited, and the modal curves are more closely spaced when compared with model 1; the multimodal energy distribution forms “streaks” and “blobs,” and the higher-order modes’ energy is dominant. For model 3 (Figure 2f), multiple modes have strong amplitude responses, and a large number of closely spaced modal curves are present; the discrete peaks of multimodal energy form an inversely dispersive trend, in which velocity appears to increase with frequency.

Note that the root-finding method, in principle, is only applicable to normally dispersive media. For an irregularly dispersive medium, the root-finding method still can be used to approximate the dispersion curves, but the layer configuration of the medium needs to simultaneously satisfy the following two conditions: (1) The half-space has the highest P- and S-wave velocity than all of the layers above and (2) the high-velocity layer within the velocity reversal section of the medium is adequately thin and thus it brings little influence on the long-period portions of the dispersion curves. Among the irregularly dispersive media shown in Figure 2 (model 2 and 3), model 2, satisfies both of these conditions; as to model 3, because its half-space does not have the highest velocity, an artificial basement whose P- and S-wave velocity is higher than those of model 3 is appended at a great depth to make the root-finding method applicable, and the top of the basement is deep enough so that the associated reflections and refractions cannot contaminate the useful portion of the wavefield. This method of appending a high-velocity basement — sometimes referred to as *locked mode approximation* (Harvey, 1981) — is useful for qualitative interpretations of the multimodal wavefield, but the quantitative accuracy of the dispersion curves is degraded to various extents.

Next, we take a closer look at the amplitude fluctuations in the dispersion spectra. When compared against amplitude responses of individual modes, it becomes evident that these fluctuations are attributable to a combination of the following factors:

1) Heterogeneous energy distribution along each individual mode: The energy distribution along a single mode is highly heterogeneous, and the modulations in energy depend strongly on the velocity structure. For instance, the fundamental mode shown in Figure 2 has distinctly different amplitude responses among the three different models, and the modulations in these amplitude responses accompany the variations of spectral amplitudes along the fundamental mode.
2) Uneven energy partitioning among modes and mode superposition: For a given velocity structure, energy partitioning is uneven among different modes, as shown by the different amplitude responses of individual modes in Figure 2b, 2d, and 2f. Moreover, when multiple modes are strongly excited, mode superposition exerts dominant control over amplitude fluctuations in the dispersion spectra. For example, in the multimodal dispersion spectra of model 2 and 3 (Figure 2d and 2f), the frequency ranges and the relative amplitudes of the spectral highlights are generally consistent with the overlaps in the modal amplitude responses, revealing strong correlations between spectral highlights and mode superposition.

In summary, the synthetic examples demonstrate striking differences in surface-wave dispersion between the normally dispersive and irregularly dispersive media. The patterns in dispersion spectra — including the dispersion trends and the fluctuations in spectral amplitudes — depend strongly on velocity structures. These three synthetic examples can be viewed as templates for identifying unusual dispersion trends observed in similar field data sets.

Field observations of surface-wave dispersion

We now examine the field data acquired at the BEO site. Visual inspection of the time-domain shot gathers (Figure 3a–3d) reveals that the low-frequency components of the wave train ($\sim$10–40 Hz) take more time than the high-frequency components ($\sim$40–130 Hz) to arrive at the receivers. This suggests that low-frequency waves propagate at lower velocities. Because these low-frequency, long-wavelength waves penetrate deeper into the ground, the field site is likely to be irregularly dispersive with embedded low-velocity features.

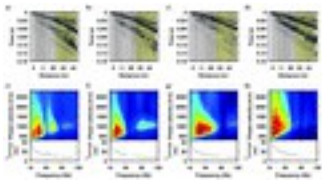

View larger version (57K)

Figure 3. Displays of the field data: The upper panels (a-d) are time-domain shot gathers (band-pass filtered with a passband of 10–130 Hz). They correspond to locations a, b, c, and d in Figure 1c, respectively. The lower panels (e-h) show the associated dispersion spectra and the principal wavelength values derived from the $(f, v_{f,v})$ points of the spectral maxima ($\lambda_{principal} = v_{maxima}/f_{maxima}$ $\lambda_{principal} = v_{maxima}/f_{maxima}$). The light-yellow patches in the upper panels show the range of the source-receiver offset (27.5–51.7 m) used for computing the dispersion spectra in the lower panels. The light-gray dots superimposed on the dispersion spectra are the $(f, v_{f,v})$ points of the spectral maxima across the frequency ranges of the spectral highlights.

Next, we apply an f-k f-k transform to the field data to produce the dispersion spectra. Zero padding is used to enhance the spectral resolution, and a Hanning taper is applied to repress artificial ripples caused by spectral leakage. As we can see from Figure 3e–3h, dispersion patterns generated from the field data are similar to the synthetic example with a high-velocity surficial layer (model 3; see the previous section). The spectral highlights are a series of discrete peaks that show an inversely dispersive trend. Such similarity between the synthetic example and the field data has important implications: First, the field data contain dominant higher-order modes, and second, the subsurface structure at the study site is inversely dispersive.

Through the dispersion analysis, the evidence points to the likely presence of embedded low-velocity features at the BEO site. Moreover, as shown in the dispersion spectra (Figure 3e–3h), the phase velocity of the low-frequency waves (10–50 Hz) varies in the range of around $300–1000 m/s$ 300–1000 m/s, which is substantially lower than literature values of $\sim 1000–2000 m/s$ ~1000–2000 m/s for frozen ground (Akimov, 1973; Tsuji et al., 2012). Note that permafrost at the BEO site is expected to reach depths of more than 300 m (Jorgenson et al., 2008), which is much deeper than the maximum penetration depths of multichannel surface-wave surveys using small impact sources.

Conventional inversion methods using dispersion curves

Conventional inversion methods seek models that can reproduce observed dispersion curves as closely as possible. The challenge in applying these methods to our field data is due to difficulties in the extraction and proper use of dispersion curves.

Depending upon how dispersion curves are retrieved during data processing and how they are used in the inversion, the conventional methods can be classified as modal-curve methods, modal-curve methods incorporating amplitude responses, and effective dispersion-curve techniques. Modal-curve methods require separation and identification of individual modes (e.g., Beaty et al., 2002; Xia et al., 2003). Although such methods are readily applicable for wavefields that are dominated by the fundamental mode, they are susceptible to mode misidentification problems when multiple modes are present (Zhang and Chan, 2003). To reduce the risk of mode misidentification, modal-curve methods incorporating amplitude responses use modal amplitude responses to aid in identifying individual modes. This method facilitates inversion for irregularly dispersive media (Lu and Zhang, 2006; Lu et al., 2007; Hayashi, 2012; Ikeda et al., 2012); a highly relevant example is the study of Tsuji et al. (2012), which identifies unfrozen zones enclosed in glacial sediments by using this method. However, two limitations are worth noting: First, this technique becomes inapplicable in situations in which modal curves cannot be unambiguously separated, and second, it does not consider the effect of data acquisition and processing procedures, even though these factors affect the modal amplitudes measured from the dispersion spectra. The last method, the effective dispersion-curve method, does not require mode identification. The spectral maxima of a dispersion spectrum at each frequency are combined into an effective dispersion curve, and then the inversion looks for models that can reproduce this observed effective curve (e.g., O'Neill et al., 2003). The method avoids mode identification and includes the effects of data acquisition and processing, but it does not fully use energy distributions of the dispersion spectra and thus relies primarily upon the kinematic characteristics of surface-wave data sets.

Whereas all the methods mentioned so far require explicit matching of observed and model-predicted dispersion curves (modal curves or effective curves) in the inversion, Maraschini et al. (2010) propose an implicit fitting procedure for multimodal dispersion curves (referred to as the Maraschini method herein). This method requires the picking of a set of multimodal dispersion curves (rather than one effective curve), but it eliminates the need for assigning mode numbers to individual curves by virtue of a novel form of the misfit function that is based upon the determinant of the Haskell-Thomson matrix: For a given model, its modal curves essentially are a set of (f_f, v_v) points at which the determinant of the Haskell-Thomson matrix goes to zero; conversely, in the Maraschini method, the inversion solves for models that can minimize the same determinant at the observed (f_f,v_v) points (i.e., all the points on the picked multimodal dispersion curves). Because the computational cost is low and no mode identification is needed, the Maraschini method has shown promise in a variety of engineering and exploration applications (e.g., Maraschini and Foti, 2010; Bergamo et al., 2011; Boiero et al., 2013). However, although mode numbering is avoided, the method still heavily relies on accurate picking of dispersion curves; hence, it becomes inapplicable when mode superposition is severe and spectral resolution is limited.

In addition to dominant higher-order modes, leaky modes further complicate the dispersion analysis and inversion for irregularly dispersive media. Velocity reversals form imperfect wave guides, in which some energy in the guided modes escapes across layer boundaries and converts to other modes, hence the name *leaky modes* (Sheriff, 2002). Physically, leaky modes cause additional modulations in the energy distributions of the wavefield. Numerically, leaky modes correspond to complex roots of the Rayleigh secular equation. Most of the existing root-finding methods for calculating dispersion curves cannot handle leaky modes directly, unless numerical approximations are applied at costs of accuracy (O'Neill and Matsuoka, 2005; Pan et al., 2013). One exception that we are aware of is the approach of Pavlakovic et al. (1997), which traces most of dispersion curves in the complex wavenumber domain. It has been used to calculate theoretical dispersion curves for nondestructive testing of pavements — an inversely dispersive medium commonly encountered in practice (Ryden and Lowe, 2004; Ryden and Park, 2004). Although calculating theoretical modal curves in the complex wavenumber domain can better capture the effect of leaky modes in the modeling step, difficulties in the accurate extraction of observed dispersion curves remain the major roadblock for dispersion-curve-based methods (Ryden and Park, 2006).

To summarize, when applied to multimodal wavefields, the limitations of the dispersion-curve-based inversion methods stem from their reliance on the kinematic characteristics of the surface-wave propagation. For irregularly dispersive media, however, the energy distribution (including the effects of higher order modes, leaky modes, and the data acquisition and processing procedure), in addition to the kinematic information, is crucial for the inversion of the multimodal surface-wave data. Therefore, we must consider applying alternative inversion methods to our field data.

Full-wavefield inversion methods using dispersion spectra

Full-wavefield methods using dispersion spectra are able to exploit the complete signal content of surface waves while avoiding mode identification requirements (Forbriger, 2003a, 2003b; Ryden and Park, 2006). Hence, we use a full-wavefield method for the inversion of our field data, and we will present the details in the next section.

A general procedure for full-wavefield inversion of surface waves

Our inversion strategy uses a derivative-free global-local search scheme to select a model that minimizes a full-wavefield objective function. The objective function is based upon the misfit between the observed and the model-predicted dispersion spectra, and the model is parameterized as a small number of horizontal layers overlying a half-space. The small dimensionality of the resulting problem allows this combination of an expensive objective function and the global-local search scheme to converge at reasonable computational costs. In this section, we describe the formula of the objective function, the hybrid search scheme, the forward modeling procedure, and the model parameterization.

Objective function: dispersion spectra misfit

The objective function takes the form of the root-mean-square deviation (RMSD):

$$M(\mathbf{m})=\sum_{i=1}^{N_f}\sum_{j=1}^{N_v}(S_{ij}-O_{ij})^2 N_f N_v, \quad \text{M(m)=∑i=1Nf∑j=1Nv(Sij−Oij)2NfNv,} \tag{1}$$

where model parameters such as layer thicknesses and S-wave velocities are the elements of the model vector $\mathbf{m}$m, MM represents the RMSD that measures the overall size of the misfit between the synthetic dispersion spectrum (SS) for an estimated model $\mathbf{m}$m and the observed counterpart (OO), N_fNf is the number of sampling

points along the ff axis (frequency) of the dispersion spectrum, and N_vNv is the number of sampling points along the vv axis (velocity) of the dispersion spectrum. Note that we apply a global normalization to the synthetic and the observed dispersion spectrum; that is, each dispersion spectrum is normalized by its maximum spectral amplitude. In this way, relative amplitudes of the dispersion spectra are preserved (no trace normalization is applied) so that the energy partitioning across the multimodal wavefield is used in the inversion. An important observation is that the evaluation of MMrequires a full-wavefield modeling operation (SS); this step is responsible for the large computational cost of our inversion approach.

Optimization techniques: Derivative-free global-local hybrid method

The inversion procedure can be posed as a bound-constrained optimization problem, for which we seek the optimal model $\mathbf{m}$m that minimizes the multivariable objective function $M(\mathbf{m})$M(m):

$$\text{minimize}_{\text{subject to}} M(\mathbf{m}); m_{(l)i} \le m_i \le m_{(u)i}, [\mathbf{m}]_n = \{m_i\} i = 1,2,\ldots,n, \underset{[m]n=\{mi\}\text{subject to}}{\text{minimize}} M(m); mi(l) \le mi \le mi(u), i = 1,2,\ldots,n, \quad (2)$$

where $m^{(l)}_i$mi(l) and $m^{(u)}_i$mi(u) denote the lower and upper bound of the search region for each model parameter, respectively.

Because the inverse problem is nonlinear, its objective function usually has multiple local minima rather than a single well-defined global minimum (Snieder, 1998; Mueller and Siltanen, 2012) and the topography of the objective-function hypersurface may be rugged or even include discontinuities. Moreover, the partial derivatives of the objective function with respect to the model parameters are not analytically available. Consequently, many commonly used algorithms that require derivative information (e.g., gradient descent and Newton's method) are inapplicable for this study.

To avoid the limitations described above, we use derivative-free approaches that only require evaluations of the objective function. Among the commonly used derivative-free methods, stochastic global-search algorithms are widely applied in surface-wave literature, including Monte Carlo methods (Socco and Boiero, 2008; Maraschini and Foti, 2010), genetic algorithms (Lu and Zhang, 2006; Lu et al., 2007; Hayashi, 2012; Ikeda et al., 2012; Tsuji et al., 2012), simulated annealing (Beaty et al., 2002; Ryden and Park, 2006), and the neighborhood algorithm (Wathelet et al., 2004; Douma and Haney, 2013). By contrast, the use of deterministic algorithms is not yet as common among surface-wave applications. Nevertheless, different from most stochastic algorithms, the performance of deterministic algorithms usually have a weaker dependence on the fine-tuning of the algorithmic parameters; the use of deterministic algorithms thus deserves further exploration for surface-wave inversion. In this study, we investigate two deterministic algorithms for the inversion of our field data, and we combine these two algorithms sequentially into a global-local hybrid approach to take advantage of their individual strengths.

Hybrid "global + local" method: This optimization approach begins with the application of the multilevel coordinate search (MCS) algorithm (Huyer and Neumaier, 1999), whose main function is to move the search toward globally optimal regions. We use a MATLAB implementation of the algorithm developed by Neumaier (2000). MCS is a largely direct method that searches for a global minimum by recursively splitting the search space into smaller subregions. The level ss, which is a rough measure of the number of times a subregion has been processed, guides a multilevel search that balances global exploration (splitting subregions with large unexplored territory) and local exploitation (splitting subregions with good objective function values). MCS also includes an optional local-search enhancement that uses surrogate models to approximate local features (i.e., model-based local search). Although this enhancement is designed to accelerate convergence, its effect in many applications is the opposite (Pošík et al., 2012): The local-search enhancement can be so slow that the maximum allowable number of function calls often is reached before a satisfactory optimum is found. Therefore, we choose to neglect this option in MCS. Instead, we use a secondary direct-search method as the local-search enhancement to improve the solution returned by MCS.

Direct local-search enhancement: The Nelder-Mead (NM) downhill simplex method is applied as an additional local-search enhancement to improve the solution obtained from MCS. The NM solver used in this study is *fminsearch*from the MATLAB Optimization Toolbox. The NM method, first introduced by Nelder and Mead (1965), is a direct local-search method. To minimize an *n*-dimensional objective function, the NM method starts with a simplex (an *n*-dimensional convex hull bounded by $(n-1)$(n−1)-dimensional hyperplanes and defined by $n+1$n+1 linearly independent vertices) constructed around a given initial "guess" (e.g., $[\mathbf{m}^0]_n$[m0]n). At each iteration, the objective function values are computed at the vertices of the simplex, and the worst vertex (with the highest objective function value among the current vertices) is found. Next, the NM method tries to replace the worst vertex by a better point to create a new simplex. Candidate replacement points are obtained by transforming the worst vertex through reflection, expansion, or contraction about the centroid of the current simplex. In this way, the NM algorithm continues to move downhill toward a local minimum. An excellent description of the NM method can be found in Press et al. (1992).

As with all local-search methods, the NM method requires a good starting model to converge toward the global optimum. By using MCS and NM in series, the MCS method provides a good starting model for the NM method — a so-called hot-start procedure, which improves the overall efficiency and accuracy of the optimization process. In the rest of this paper, we use *MCS-NM hybrid method* as the name of the optimization techniques (Appendix A contains a list of the key parameters used in the optimization).

Forward modeling of the wavefield and parsimonious model parameterization

Forward modeling of the wavefield is a two-step procedure: A synthetic shot gather is first generated for a given model using the same acquisition geometry as the field data; the shot gather is then transformed into a dispersion spectrum. Because the computation of the synthetic shot gather is time consuming, and the number of model parameters needs to be relatively small for the selected optimization method, we adopt a parsimonious parameterization of the velocity structure that is represented as a horizontally layered elastic model. Although viscoelastic media are likely to be more realistic representations of the subsurface, elastic models are used to avoid increasing the problem dimension. The validity of using elastic inversion will be addressed in a later section.

Specific settings for the field-data application

Key parameters determined from the observed dispersion spectra: The optimal f-vf-v window and the investigation depths

To apply the full-wavefield inversion to the field data, we first need to tailor the setup of the inversion according to some key parameters that are determined from the observed dispersion spectra, namely, the spectral range of the usable field-data signals, which dictates the optimal f-vf-v window used for evaluating the objective function (equation 1), and the range of investigation depths allowed for the field data, which serves as prior information for the model parameterization. This section provides details about these key parameters.

First, based upon the dominant energy distributions of the observed dispersion spectra, we select the optimal f-vf-vwindow used in the inversion: The frequency range is 10–130 Hz, and the velocity range is $300–2800 m/s$300–2800 m/s(Figure 3).

Next, in preparation for assessing the investigation depths allowed for the field data, we estimate the range of resolvable wavelengths using three criteria: the signal content of the dispersion spectra, the spatial sampling of the acquisition geometry, and the principal wavelengths associated with the spectral maxima. The signal content of the dispersion spectra, bounded by the optimal f-vf-v window, allows us to make a first-order estimate of the range of the detectable wavelengths, which is $\sim 2–200 m$~2–200 m ($\lambda^{min}=v^{min}/f^{max}$λmin=vmin/fmax; $\lambda^{max}=v^{max}/f^{min}$λmax=vmax/fmin). Within this range, however, only a subset of the wavelengths is practically resolvable, owing to the limited spatial sampling that is dictated by the acquisition geometry: Receiver spacing (ΔxΔx) of 1.1 m yields a minimum resolvable wavelength ($\lambda^{min}\approx\lambda^{Nyquist}=2\Delta x$λmin≈λNyquist=2Δx) of $\sim 2 m$~2 m, and the total array length determines a maximum resolvable wavelength ($\lambda^{max}\approx x^{max}$λmax≈xmax) of $\sim 50 m$~50 m. In addition, the principal wavelengths of the wavefield — estimated based upon the (f,vf,v) points of spectral maxima by using $\lambda^{principal}=v^{maxima}/f^{maxima}$λprincipal=vmaxima/fmaxima — also provide complementary constraints for the range of the resolvable wavelengths. As shown in Figure 3e–3h, the maximum value of the principal wavelengths is around 50 m, which is consistent with the maximum resolvable wavelength dictated by the array length. In short, the range of the resolvable wavelengths is $\sim 2–50 m$~2–50 m.

Then, by following the one-half wavelength rule of thumb, we can assess the range of investigation depths based upon the range of the resolvable wavelengths: Assuming a scaling factor of one-half between the resolvable wavelengths and the associated resolvable depths (defined as the depth at which V^SVS can be resolved with reasonable accuracy) (Rix and Leipski, 1991; Park et al., 1999), the range of the investigation depths is $\sim 2–25 m$~2–25 m. Note that such rules are primarily applicable to fundamental-mode surface waves. By comparison, higher order modes have stronger sensitivity to deeper units than the fundamental mode of the same wavelength (Xia et al., 2003); hence, the maximum investigation depth for our field data may extend deeper, especially for detecting the strong contrast between frozen and unfrozen strata.

Forward modeling of the full wavefield: The source wavelet and the Green's function

In this study, the zero-offset trace of each shot gather is used as an empirical source wavelet. Strictly speaking, the zero-offset trace itself already is the convolution of the true source wavelet and the Green's function. Nevertheless, because the Green's function is not known prior to the inversion, the true source wavelet cannot be effectively retrieved. Despite this limitation, the zero-offset trace performs well as the source wavelet, especially in providing the appropriate frequency content and wave shapes for the model-predicted wavefield.

For each shot gather, the Green's functions in response to a vertical point force (mimicking the sledgehammer impact) are generated by the wavenumber integration method (also referred to as the reflectivity method or the discrete wavenumber method in seismology literature) (Herrmann, 2004), which is a full-wavefield technique applicable to horizontally layered media. In the end, to complete the wavefield computation, the Green's function is convolved with the source wavelet to produce a synthetic shot gather.

Parsimonious model parameterization: Two layers over a half-space elastic model

We adopt an elastic model comprising two uniform layers over a half-space for a parsimonious subsurface representation. In addition to computational efficiency considerations, the rationales for this parameterization also come from characteristics of the wavefield and prior knowledge of the subsurface structure.

The horizontally layered model is a reasonable abstraction of the subsurface because of the characteristics of the observed wavefield. Surface waves are primarily sensitive to average velocity structures underneath the source and the receiver array. This assumption may not be valid when marked lateral variations or heterogeneities are present, as surface waves could be back propagated by lateral velocity variations or backscattered by short-wavelength heterogeneities (e.g., Yilmaz and Kocaoglu, 2012). In the recorded data, this back propagation and back scattering could in turn manifest as wavefield distortions that carry the signatures of the localized variations and heterogeneities. The field data in the frequency range of 10–130 Hz, however, do not show such distortions in either the x-tx-t or f-kf-k domain. Although lateral variations and heterogeneities inherently exist in the subsurface, the horizontally layered model is a justifiable simplification of the velocity structures concerning the inversion of our field data.

Prior knowledge is a combination of geologic and geophysical information. Geologic prior information come from existing studies examining soil cores from Barrow, which suggest an ice-rich uppermost layer. Geophysical prior information are derived from the results of an electric resistivity tomography (ERT) profile along the same survey line, which can be simplified as a two-layer structure consisting of a high electric resistivity layer at the top ($>2500 ohm-m$>2500 ohm-m; the thickness varies from 0.5 to more than 5 m) and an underlying low electric resistivity layer (as low as $\sim 10 ohm-m$~10 ohm-m) (Hubbard et al., 2013). In this way, the two layers in the seismic velocity structure correspond to the high and the low electric resistivity features. However, ERT loses resolution for structures deeper than 6 m below the surface because of its limited depth penetration in this particular case (B. Dafflon, personal communication, 2012), whereas the seismic surface waves used in this study allow a maximum investigation depth of at least 25 m (detailed in an earlier section titled “Key parameters determined from the observed dispersion spectra: The optimal f-vf-v window and the investigation depths”). For the purpose of increasing the depth extent of the geophysical investigation, as well as providing independent information for the subsurface characterization, the seismic velocity model includes a half-space beneath the two-layer structure.

SYNTHETIC TESTS

To test the validity of our full-wavefield inversion approach, we conduct a series of tests using synthetic data generated from a reference model. The main objectives of the synthetic experiment are to determine model parameters for the inversion based upon the results of the sensitivity analysis and to examine the performance of the MCS-NM hybrid method.

The reference model and its wavefield

We use two layers over a half-space model shown in Table 1 as the reference model. Note that we specifically design this model to be irregularly dispersive. To match the frequency content of the synthetic data with that of the field data, we use one of the empirical source wavelets (with a centroid frequency of 68 Hz and a half-peak bandwidth of 13–82 Hz) obtained from the field data as the source wavelet for the synthetic tests. We then convolve this source wavelet with the Green’s function of the reference model to construct the reference wavefield.

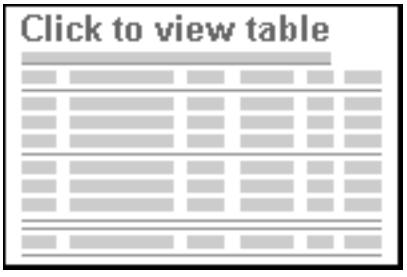

View Larger Version

Table 1. Reference two layers over a half-space elastic model.

Sensitivity analysis of the model parameters

To determine how many model parameters should be used and which parameters are significant, we first examine the objective function's sensitivity to different model parameters. Considering only the elastic properties, we begin with eight candidate model parameters h^1h1, V^{S1}VS1, V^{P1}/V^{S1}VP1/VS1, h^2h2, V^{S2}VS2, V^{P2}/V^{S2}VP2/VS2, V^{S3}VS3, and V^{P3}/V^{S3}VP3/VS3 (where $h$hdenotes the layer thickness; V^PVP denotes the P-wave velocity; V^SVS denotes the S-wave velocity; and the subscripts 1, 2, and 3 denote the top layer, the middle layer, and the half-space, respectively) and examine their contributions to the objective function.

We first look into the influence of each candidate model parameter by examining 1D cross sections of the objective function (equation 1). We perturb each of the model parameters by $\pm 50\%$±50% relative to its reference value while keeping the remainder of the seven parameters fixed. The results are shown in Figure 4. In each of the 1D cross sections, the depth and sharpness of the "valley" is proportional to the sensitivity of the corresponding model parameter. Three observations can be extracted from this synthetic test: First, the asymmetric shape of each valley and the varying depths of these 1D cross sections suggest that different parameters contribute differently to the objective function; second, many of these 1D cross sections contain "quasiplateaus" — flat portions of the objection function that are nearly insensitive to perturbations in model parameters (e.g., the nearly flat portions of the 1D cross section in Figure 4b, 4f, 4g, and 4h), suggesting the ill-posed nature of the inverse problem; third, V^{P3}/V^{S3}VP3/VS3(the V^P/V^SVP/VS ratio of the half-space) is the least sensitive parameter among all the candidate model parameters, and thus it is not used in the inversion. The number of candidate model parameters is now reduced to seven (h^1h1, V^{S1}VS1, V^{P1}/V^{S1}VP1/VS1, h^2h2, V^{S2}VS2, V^{P2}/V^{S2}VP2/VS2, and V^{S3}VS3).

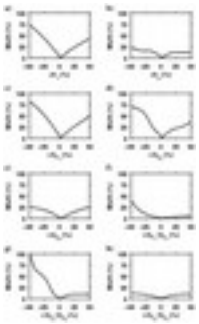

View larger version (37K)

Figure 4. The 1D cross sections of the objective function $M(\mathbf{m})$M(m) (equation 1). The vertical axes correspond to the normalized misfit. The horizontal axes correspond to relative parameter perturbations in the range of $\pm 50\%$±50% with respect to the reference values (zero values correspond to reference values in Table 1).

We then examine 2D cross sections of the objective function to learn more about the characteristics of the inverse problem. We group model parameters into pairs and simultaneously perturb each parameter pair by $\pm 45\%$ ±45%relative to the reference value while keeping the other five parameters fixed. Results obtained from six of these parameter pairs are shown in Figure 5. Three characteristics of the inverse problems are illustrated by this test: First, quasi-plateaus are present in these 2D cross sections (e.g., the nearly flat portions of the 2D cross section in Figure 5d and 5e), again suggesting that the inverse problem is ill posed; second, the objective function has local minima, which indicates the necessity of using global-search methods for the inversion; and third, the model parameters are correlated (e.g., the curved valley in Figure 5a) and thus the inverse problem is inseparable.

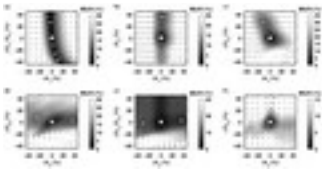

View larger version (65K)

Figure 5. The 2D cross sections of the objective function $M(\mathbf{m})$M(m) (equation 1). The horizontal and vertical axes correspond to relative parameter perturbations in the range of $\pm 45\%$±45% with respect to the reference values shown in Table 1. The varying shades of gray represent the values of the misfit function. The color scale is clipped at 40% of the maximum misfit-function value for each cross section. Gray vectors indicate the gradient of the objective function with their lengths and directions. Valleys and local minima (labeled with white dots) are visible. The global

minima are marked by white stars.

Although examining the objective functions within a higher dimensional context could provide more information, it is difficult to visualize and expensive to compute. The 1D and 2D cross sections of the objective function, though incomplete, already provide enough knowledge for us to make decisions on what model parameters to use in the inversion.

Among the seven candidate model parameters, we can eliminate one more parameter: Because we can use first arrivals of the field data to determine the P-wave velocity of the top layer (V^{P1}VP1), we do not directly invert for V^{S1}VS1. Instead, we invert for V^{P1}/V^{S1}VP1/VS1, and from there, we then obtain V^{S1}VS1 by using the relation $V^{S1}=V^{P1}/(V^{P1}/V^{S1})$VS1=VP1/(VP1/VS1).

To summarize, the sensitivity analysis helps us to make the decision on model parameters that will be inverted for: They are six parameters consisting of h^1h1, V^{P1}/V^{S1}VP1/VS1, h^2h2, V^{S2}VS2, V^{P2}/V^{S2}VP2/VS2, and V^{S3}VS3.

Performance test of the full-wavefield method

To examine the performance of the MCS-NM hybrid method, we conduct full-wavefield inversion using the dispersion spectrum of the reference model (Table 1) as the synthetic data. We first launch the MCS solver starting from search bounds shown in Table 2. After 327 iterations, MCS converges to an optimum with 70% of misfit reduction. Then, starting from the MCS solutions, we use the NM solver for the local-search enhancement. After 361 additional iterations, we successfully obtain the globally optimal solutions with the NM solver (Table 1). The entire inversion procedure takes approximately 2.5 h (wall-clock time) on a Linux workstation equipped with a quad-core 3.07 GHz Intel Xeon processor. The iteration history of the MCS-NM hybrid method is shown in Figure 6a. The convergence improvement generated by the NM local-search enhancement is evident.

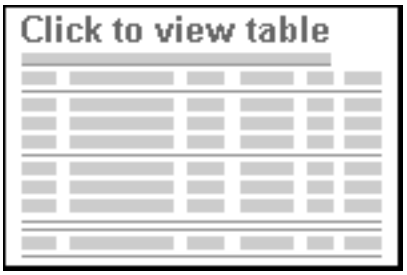

View Larger Version

Table 2. Search bounds of MCS for the synthetic experiment.

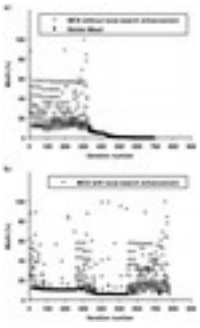

View larger version (38K)

Figure 6. Performance comparison between the MCS-NM hybrid method and the MCS method with local-search enhancement: (a) iteration history of the MCS-NM hybrid method and (b) iteration history of the MCS method with local-search enhancement (the maximum allowable number of iterations is set as 5).

To gain insight into the performance of the optional local-search enhancement in MCS, we also conduct an additional inversion run with the same search bounds but using MCS with local-search enhancement rather than the MCS-NM hybrid method. To avoid excessively long runtime spent in the local-search enhancement step, we use a strong

constraint on the local-search parameter (the maximum number of local searches is set as 5). Even with this constraint, MCS still spends a large number of iterations on the local search. After 776 iterations, which is 88 iterations more than the total number of iterations used by the MCS-NM hybrid method, MCS still does not converge to an optimum of the same quality as the one obtained from the MCS-NM hybrid method (Figure 6b).

In summary, the results of the synthetic experiment indicate the validity of the full-wavefield method and that the use of the MCS-NM hybrid method brings marked improvements to the optimization procedure.

Effects of noise and attenuation on the full-wavefield inversion

In contrast to the error-free synthetic example shown above, inversion of field data is always subjected to data errors and model errors. Data errors can be introduced from a variety of sources, including random (e.g., wind, electric spikes) and coherent noise (e.g., scattering from lateral heterogeneity) sources. Model errors occur when the model parameterization, owing to its simplicity, is insufficient for describing a subsurface that is inherently complex and heterogeneous. Because data and model errors are inevitable in real inversion, we need to test the robustness and validity of the full-wavefield method in the presence of these errors. For this purpose, we conduct a series of synthetic tests to examine the effects of random noise — one representation for data errors, as well as possible biases introduced by neglecting viscoelastic attenuation — a probable source of model errors, on the full-wavefield inversion.

Effects of random noise

The synthetic example described previously shows the best attainable results because the data are noise-free. To examine whether the inversion is robust in the presence of noise, we carry out a series of tests using the same reference model as what is used in the noise-free test (Table 1): We first generate two sets of noisy synthetic data by adding 20% and 45% Gaussian noise to the noise-free synthetic data, for which the two noise levels are chosen to be comparable to and worse than that of the field data, respectively (Figure 7). We then invert these two sets of noisy data using the full-wavefield method. Model parameters inverted from these noisy data (Table 3) show slight deviations from the reference values — as expected in the presence of noise contamination. However, the amount of deviation is very low (no larger than 4.8%), which demonstrates the robustness of the method in the presence of Gaussian random noise.

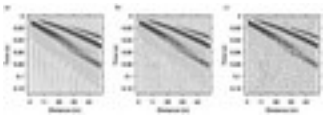

View larger version (59K)

Figure 7. Synthetic data sets: (a) Noise-free shot gather generated by wavenumber integration method using reference model parameters listed in Table 1. Gaussian noise of 20% and 45% is added to the same shot gather, resulting in an S/N of (b) 14 dB and (c) 7 dB (the $S/N=10\log_{10}(\sum_{i=1}^{N_t}A_{Si}^2/\sum_{i=1}^{N_t}A_{Ni}^2)$ $S/N=10\log_{10}(\sum_{i=1}^{N_t}A_{Si}^2/\sum_{i=1}^{N_t}A_{Ni}^2)$, where A_S A_S denotes the amplitude of the signal, A_N A_N denotes the amplitude of the noise, and N_t N_t denotes the total number of points in each trace of the shot gather).

Click to view table

View Larger Version

Table 3. Model parameters inverted from noisy synthetic data.

Effects of viscoelastic attenuation

The synthetic examples shown above consider purely elastic models. Nevertheless, near-surface sediments are often strongly attenuating — a factor that could significantly modulate the energy distributions of dispersion spectra, and thus a simultaneous inversion of velocity and attenuation structures may seem attractive. For such an inversion, however, the increased problem dimensionality can dramatically increase runtime of the direct-search method. For this reason, although neglect of attenuation can potentially introduce biases to the resulting velocity structure, elastic

inversion is often selected for computational efficiency reasons. In this section, we explore probable ranges of attenuation within which elastic inversion remains viable — in the context of near-surface structures in permafrost.

To investigate the validity of our elastic inversion strategy in the presence of attenuation, we conduct a series of elastic inversions to invert synthetic data generated from viscoelastic models. We then compare the inverted velocity structure against the reference values to examine the extent of biases introduced by the neglect of attenuation. Based on the same reference model shown in Table 1, we first construct viscoelastic models for this test by assigning uniform quality factor Q (assuming $Q^P = Q^S$ QP=QS for P- and S-waves) to each layer. Following the heuristic rule that high velocities often accompany high Q values, and vice versa, we use a high Q value for the high-velocity top layer and a low Q value for the low-velocity middle layer and the low-velocity half-space (i.e., $Q^1 > Q^2 = Q^3$ Q1>Q2=Q3). We fix the high Q value at 200, which is comparable to field-measured Q values of ~ 250 ~250 for hydrate-rich sediments (Sain et al., 2009; Sain and Singh, 2011) — here used as an analog for ice-rich permafrost. Next, we vary the low Q value between 10 and 50 so as to evaluate the range of Q values within which elastic inversion can recover model parameters with satisfactory accuracy, despite the presence of attenuation.

The test results (Table 4) indicate that elastic inversion remains accurate (with biases no greater than 5.7% in the inverted model parameters) if the low Q value of the viscoelastic model does not fall below ~ 24 ~24. This lower limit of Q for applying elastic inversion is within the range of Q values bounded by the two "end-member" sediments (surficial water-saturated sands and silt-clays) as summarized in Hamilton (1976): Q^P QP of 24–45 and Q^S QS of 7–31 for sands; and Q^P QP of 105–314 and Q^S QS of 10–31 for silt-clays (mud). These ranges of Q values are likely to be comparable to Q values in ice-poor permafrost (e.g., partially frozen or unfrozen permafrost). Considering the lower limit of ~ 24 ~24 for Q, the elastic inversion remains valid unless very low Q values are present. In this study, we only consider elastic inversion by assuming that very low Q values are absent in permafrost structures relevant to our field site.

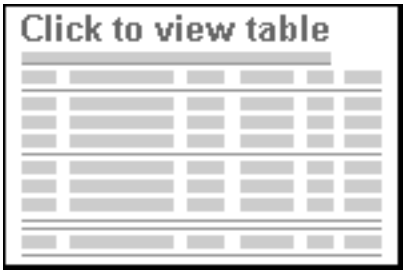

View Larger Version

Table 4. Model parameters obtained from elastic inversion of the synthetic data that are generated from viscoelastic models.

After validating the full-wavefield method through the synthetic tests, we apply it to the inversion of our field data acquired at the BEO site.

Performance evaluation of the full-wavefield method

We first evaluate the performance of the optimization procedure in the field-data experiment. Starting with the search bounds shown in Table 5, the total number of iterations range from 570 to 950 for a given shot gather, which corresponds to around 4–11 h of runtime (wall-clock time). Figure 8 shows an example of the iteration history obtained from the shot gather corresponding to section b in Figure 1c. Similar to the algorithmic behavior observed in the synthetic experiments, the MCS-NM hybrid method balances global exploration and local exploitation. Although the overall patterns of the iteration history are similar to the synthetic case, the hybrid method, when applied to the field data, generally spends a larger number of iterations on broad MCS exploration in comparison to the iterations required for the NM local-search enhancement. This may be explained by the more rugged objective-function hypersurface as expected in the presence of data error.

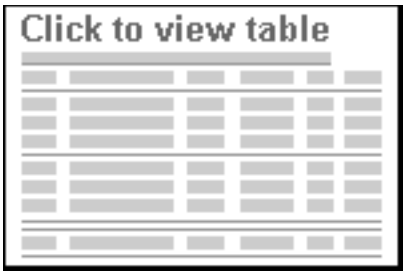

View Larger Version

Table 5. Search bounds of the multilevel coordinate search solver used in the field-data experiment.

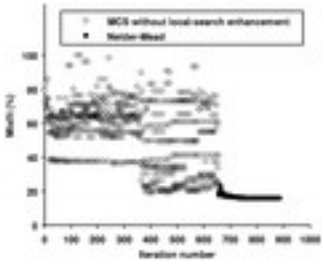

View larger version (54K)

Figure 8. Iteration history of the MCS-NM hybrid method when applied on the field data acquired at section b of the survey line (see Figure 1c).

Next, we check the quality of the optimal solutions by examining the resultant data fits. Moreover, even though the inversion is based upon dispersion spectra in the f-vf-v domain, we also examine the waveform fit in the x-tx-t domain. A representative example of the data fits is given in Figure 9 (corresponds to section b of the survey line shown in Figure 1c). In the f-vf-v domain (Figure 9d and 9e), the dominant "two-patch" pattern of the dispersion spectra is consistent between the synthetic and observed dispersion spectra. For the low-frequency components (∼10–50Hz∼10–50 Hz), although differences are present between the energy distribution of the synthetic and observed spectra (as shown by the orange and light blue patches in Figure 9f: The spectral highlight of the observed spectrum is more narrow-banded and slightly richer in the frequency content of ∼10–13Hz∼10–13 Hz than the synthetic spectrum), the shape and position of the spectral highlights match well between the model prediction and the real data; but for the high-frequency components (∼60–130Hz∼60–130 Hz), the position of the spectral highlight is shifted in the synthetic spectrum, yielding the associated differences shown in Figure 9f (the orange and light blue patches). Likewise, in the x-tx-t domain (Figure 9a–9c), although the strong low-frequency wavelets are in good agreement between the synthetic and observed shot gathers, the weaker high-frequency wavelets are not well aligned. Such discrepancies in the high-frequency components, though undesirable, are expected because they are fairly weak in the wavefield and thus are more susceptible to biases in the inversion. Despite the less satisfactory fit to the high-frequency portion of the wavefield, the optimal model is able to predict the presence, shapes, and relative amplitudes of the major wavelets in the x-tx-t domain, even though no direct waveform fitting is used in the inversion.

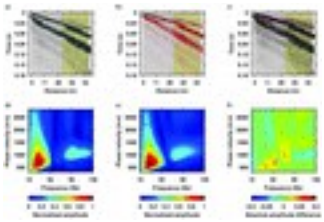

View larger version (67K)

Figure 9. Example of data fits for the field data (section b in Figure 1c): The top panels show x-tx-t domain displays (i.e., shot gathers) for the (a) observed wavefield, (b) synthetic wavefield, and (c) overlay of the observed and the synthetic wavefields. The light-yellow patches show the range of the source-receiver offset (27.5–51.7 m) used for computing the dispersion spectra. The bottom panels show f-vf-v domain displays (i.e., dispersion spectra) for the (d) observed

wavefield, (e) synthetic wavefield, and (f) difference between the observed and the synthetic wavefields.

To summarize, the full-wavefield approach converges appropriately when applied to the field data. Even though the method is based upon dispersion spectra other than direct waveform fitting, the model-predicted wavefield compares well with the observed counterpart in both the x-tx-t and the f-vf-v domains.

Results: Permafrost models with embedded low-velocity zones

After confirming the effectiveness of the full-wavefield method when applied to the field data, we conduct the six-parameter inversion to invert the data. Here, we examine the resulting models in this section.

To gain knowledge about the vertical and lateral characteristics of the inverted S-wave velocity structures, we compile the model estimates into Table 6. The most striking features shared by these model profiles are the pronounced low-velocity zones (~ 300–$680\,\mathrm{m/s}$~300–680 m/s) that underlie the thin high-velocity top layer (with velocities of ~ 1700–$2600\,\mathrm{m/s}$~1700–2600 m/s and thicknesses of ~ 3.5–$4\,\mathrm{m}$~3.5–4 m). We cannot resolve the maximum depths of the low S-wave velocity zones because of the limited investigation depths of the wavefield, but we are confident that these zones extend at least down to $\sim 25\text{-}\mathrm{m}$~25-m below the surface.

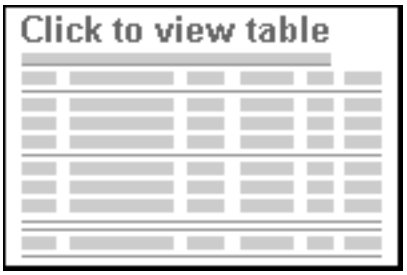

View Larger Version

Table 6. Model parameters inverted from the field data.

To evaluate the extent to which we can constrain the model estimates obtained from the inversion, we compute approximate uncertainty envelopes in the following way: We perturb each model estimate around its original value and compute the corresponding objective-function values for the perturbed model profiles Next, we choose threshold objective-function values that are 10% larger than the minimum misfit. Finally, we use the parameter values associated with the misfit threshold as the upper and lower bounds of the uncertainty envelopes. Here, we report minimum and maximum bounds of the parameters among all four sections listed in Table 6:
(1) $-0.5^{-0.5}$ to $+1.2\,\mathrm{m}^{+1.2}$ m for h^1h1, (2) $-0.35^{-0.35}$ to $+0.70^{+0.70}$ for V^{P1}/V^{S1}VP1/VS1 (translates to -880^{-880} to $+830\,\mathrm{m/s}^{+830}$ m/s for V^{S1}VS1), (3) $-16.5^{-16.5}$ to $+8.0\,\mathrm{m}^{+8.0}$ m for h^2h2, (4) -107^{-107} to $+182\,\mathrm{m/s}^{+182}$ m/s for V^{S2}VS2, (5) $-0.45^{-0.45}$ to $+0.35^{+0.35}$ for V^{P2}/V^{S2}VP2/VS2, and (6) -70^{-70} to $127\,\mathrm{m/s}^{127}$ m/s for V^{S3}VS3. In all six parameters, h^2h2 carries the largest uncertainty. This is mainly due to the very small velocity contrast between the middle layer and the half-space (both layers have velocities that are much lower than the top layer), which yields the low sensitivity of the objective function with respect to h^2h2, and it is consistent with the appearance of the 1D objective-function cross section demonstrated in the synthetic experiment (Figure 4b). The V^{S1}VS1 values also have large uncertainties, which could be a result of the method's relatively low sensitivity to the high-frequency portion of the wavefield. Velocity values of the low-velocity zones (V^{S2}VS2 and V^{S3}VS3), however, have narrow uncertainty envelopes and thus are well constrained.

We also qualitatively evaluate the model estimates by comparing the seismic velocity models with results obtained from a different geophysical method — the ERT profile (Figure 10). Although the boundaries between high- and low-velocity layers do not match the boundaries between high- and low-resistivity features in a precise fashion, the first-order layering structures between the seismic velocity (V^SVS) and electric resistivity are in general agreement.

Furthermore, the consistent results between these two different geophysical methods indicate that the low-velocity zones are likely to also have very low electric resistivity ($\sim 10\,\mathrm{ohm\text{-}m}$~10 ohm-m) (Hubbard et al., 2013).

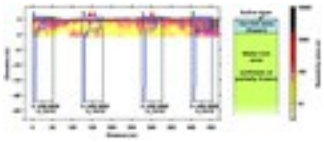

View larger version (28K)

Figure 10. Comparison of S-wave velocity profiles and the ERT results (Hubbard et al., 2013). Shear-wave velocity (Vsvs) profiles a-d correspond to locations shown as sections a-d in Figure 1c. The red triangles show the locations of the three core samples. The schematic on the right shows the conceptual permafrost model with embedded water-rich zones.

Beyond the first-order layering, more detailed comparisons between the ERT profile and the seismic models are neither possible nor meaningful at this point. This is because of their fundamentally different inversion schemes and their different sensitivities to water-content changes. First, the ERT profile is intrinsically smooth as a result of the second-order Tikhonov regularization used in the tomographic inversion; whereas seismic profiles based upon a layered-model parameterization (two layers over a half-space) present the subsurface as distinct layers. Second, for a given amount of changes in water content, electric properties (strongly depend on fluids that carry ions) generally show more pronounced variations than seismic properties (mainly transmit energy through the solid matrix of the medium); such sensitivity difference could be amplified in the presence of dissolved salts.

In addition, seasonal differences in the acquisition time further impede an exact comparison between the ERT profiles and the seismic models. The electric resistivity data were acquired near the end of the thaw season at Barrow (the end of September) (Hubbard et al., 2013), whereas the seismic data were acquired near the end of the freeze season (mid-May). In response to the atmospheric temperature changes, seasonal variations in ground temperatures, though decreasing with increasing depths, are present from the surface all the way down to ~15–20-m~15–20-m below the surface (V. Romanovsky, personal communication, 2013). As a result, the boundary between the shallower and deeper permafrost layers could vary in response to these seasonal changes. Because electric resistivity is much more sensitive to small changes in water content than seismic velocities, especially in the presence of dissolved salts, a detailed comparison between the ERT profile and the seismic models is not possible.

Despite that an exact comparison is presently unfeasible, the consistency in the first-order layering between the ERT profile and the seismic models provides key information about the permafrost subsurface — particularly, the presence of the embedded low-velocity and low-resistivity zones that may only be partially frozen or unfrozen. Moreover, it suggests the possibility for a joint inversion of concurrent seismic and electric data in the future.

Given the subzero ground temperatures, around −8°C−8°C to −10°C−10°C in nearby boreholes in the depth range of ~3–25m~3–25 m (V. Romanovsky, personal communication, 2012), the low-velocity zones at depth are unusual features: These well-constrained zones exhibit S-wave velocities that are as low as 300–680m/s300–680 m/s, whereas ordinarily S-wave velocity of ice-rich frozen ground should be close to the velocity in pure ice (~1800m/s~1800 m/s) (Tsuji et al., 2012). The low S-wave velocity values could be reasonable in ice-depleted ground that is either dry or water saturated. But the low-velocity zones of our study site are not likely to be dry because of the collocated low electric resistivity values (~10ohm-m~10 ohm-m — about 10–1000 times lower than typical values observed in permafrost). As a result, low values in electric resistivity and seismic velocity point to an alternative interpretation: These embedded low-velocity zones are likely to be water-rich ground that are saturated with water or an ice/water mixture.

Under subzero temperatures of −8°C−8°C to −10°C−10°C, high salt content is a plausible mechanism for preventing water from freezing through its freezing-point depression effect. For example, assuming that the dissolved salts are made entirely of NaCl, a pore-water salinity of 140g/L140 g/L (four times of the typical seawater salinity) can lower the freezing point of soils down to −8°C−8°C according to the empirical equation developed by Velli and Grishin (1983)(Appendix B). Therefore, the low-velocity (and low-resistivity) zones may contain saline pore waters

and thus remain perennially unfrozen or only partially frozen under subzero temperatures. The salts could have originated from seawater contained in marine deposits — the predominant source of the unconsolidated sediments at Barrow (Black, 1964). In extreme cases, the salt content may be sufficiently high that these saline layers or zones remain perennially unfrozen while still constituting part of the permafrost (a class of features often referred to as *cryopegs*in permafrost literature).

Subsequent to the surface-wave acquisition campaign, three core samples were extracted along the same survey line (see the symbols in Figure 10; the core depths are 1.65, 2.55, and 3.10 m, respectively), which provide evidence in support of the presence of saline pore waters at depth. These three cores, apart from the differences in the depth extent of their ice-rich top sections, have broadly similar profiles with partially frozen basal sections starting from the depths of around 1.4–2.6 m. Preliminary core-sample analysis shows that the electric conductivity of the pore fluid extracted from the partially frozen section is as low as $1.5–2.0 S/m$1.5–2.0 S/m (equivalent to a resistivity range of 0.5–0.7 ohm-m; comparable to typical seawater resistivity of $\sim 0.2 ohm-m$~0.2 ohm-m) (B. Dafflon, personal communication, 2014). Despite the fact that these core samples do not reach deep enough to directly sample the embedded low-velocity zones that are uncovered by our surface-wave data, the saline basal sections are suggestive of a pronounced saline-permafrost zone at depth. In addition, prior studies have reported many observations of cryopegs and/or saline permafrost in the Barrow vicinity (e.g., O'Sullivan, 1966; Brown, 1969; Williams, 1970; Yoshikawa et al., 2004; Meyer et al., 2010). Therefore, the presence of saline permafrost appears to be the most plausible cause for the observed low-velocity zones.

The extensive presence of saline permafrost at the BEO site, if confirmed, may impact the estimates of organic carbon degradation as well as biogenic gas fluxes (CO^2CO2 and CH^4CH4) from deeper permafrost strata. Because substantial amount of water remains liquid in saline permafrost at subzero temperatures, cold-adapted microorganisms could maintain metabolisms with the aid of liquid water. Studies by Gilichinsky et al. (2005), for example, have found active microorganisms in marine cryopegs from Siberia that may have survived for 43,000 years at $-10°C$−10°C.

In addition to seismic field survey and deep coring, laboratory testing of seismic velocities in saline permafrost could provide rock-physics insight to facilitate seismic interpretation efforts. Several previous laboratory studies have approached the effect of dissolved salts in consolidated permafrost (Pandit and King, 1979), unconsolidated permafrost (King et al., 1982; Matsushima et al., 2011), and ice-brine mixtures (e.g., Spetzler and Anderson, 1968; Matsushima et al., 2008). Although they all come to the consensus that freezing-point depression of salts can keep seismic velocities low even at subzero temperatures, the salinities used in these studies is generally low (mostly lower than typical seawater salinity) and the range of the tested salinity is quite narrow.

Choose Top of page

CONCLUSION

Abstract INTRODUCTION BACKGROUND METHODS SYNTHETIC TESTS FIELD DATA INVERSION DISCUSSION CONCLUSION <<ACKNOWLEDGMENTS REFERENCES APPENDIX A PARAMETER SETTI... APPENDIX B EMPIRICAL EQUAT... CITING ARTICLES

In summary, our study demonstrates that the dispersion analysis and the full-wavefield inversion of surface waves are effective for detecting and delineating embedded low-velocity zones in permafrost. Although surface-wave methods are generally applicable even when velocity reversals are present in the ground (i.e., seismic velocities do not always increase with depths), velocity reversals embedded in permafrost can be unusually drastic, considering the large velocity contrasts ($\sim 70%–80%$~70%–80%) between the frozen and unfrozen materials. Consequently, higher-order modes dominate the wavefield and leaky modes further complicate the energy distributions in the wavefield. In this case, it is impossible to identify or pick individual surface-wave modal curves and thus the conventional, dispersion-curve-based inversion methods become unsuitable. In contrast to the conventional methods, the full-wavefield approach used in our study does not rely on individual modal curves. Moreover, our method uses the complete signal content of the wavefield — including higher-order modes, leaky modes, the energy distribution, and all the acquisition and processing effects — to constrain the velocity structures. With the full-wavefield method, we are able to infer embedded low-velocity zones from inversely dispersive surface-wave data acquired from our study site at Barrow, Alaska. The low-velocity zones may correspond to saline unfrozen or partially frozen zones enclosed in permafrost.

Our full-wavefield approach is currently limited by the high computational cost, the nonlinear nature of the inverse problem, and the simplicity of model parameterization. Computing the full wavefield is much more time-consuming than computing modal curves. The irregular and possibly drastic velocity variations in permafrost also increase the nonlinearity of the inverse problem, which yields slow convergence of the optimization procedure. Lastly, to alleviate "the curse of dimensionality" (with increasing number of model parameters, runtime rapidly increases whereas the quality of the solutions deteriorates), parsimonious model parameterization must be used. As a result, velocity models obtained through the full-wavefield method are simple and thus fine-scale features may not be effectively resolved.

Despite these limitations, the full-wavefield method is a promising technique for quantitative delineation of permafrost. Embedded low-velocity zones, which are challenging imaging targets for conventional seismic prospecting, can be effectively inferred from the field data. The resulting velocity models, although simple, provide key information about physical properties of the subsurface. In addition, if more detailed velocity structure is desirable, the full-wavefield method could provide starting models for further refinement via techniques such as classical time- and frequency-domain waveform inversion.

ACKNOWLEDGMENTS

Choose Top of pageAbstractINTRODUCTIONBACKGROUNDMETHODSSYNTHETIC TESTSFIELD DATA INVERSIONDISCUSSIONCONCLUSIONACKNOWLEDGMENTS <<REFERENCESAPPENDIX APARAMETER SETTI...APPENDIX BEMPIRICAL EQUAT...CITING ARTICLES

As part of the Next-Generation Ecosystem Experiments (NGEE-Arctic) project sponsored by the Office of Biological and Environmental Research in the DOE Office of Science, this study is supported through contract DEAC0205CH11231 to Lawrence Berkeley National Laboratory and through contract DE-AC05-00OR22725 to Oak Ridge National Laboratory. We thank S. Hubbard (Lawrence Berkeley National Laboratory) and S. Wullschleger (Oak Ridge National Laboratory) for their leadership within the NGEE-Arctic program. We also thank J. Peterson, B. Dafflon, C. Ulrich (all of Lawrence Berkeley National Laboratory), and A. Gusmeroli (University of Alaska, Fairbanks) for their generous help in performing the seismic survey in the harsh field environment at Barrow. We appreciate the valuable suggestions offered by D. Dreger (University of California, Berkeley) and R. Herrmann (Saint Louis University). M. Robertson (Lawrence Berkeley National Laboratory) provided substantial assistance in making maps of the study site. B. Dafflon significantly assisted our analysis by providing preliminary data on the core samples relevant to this study. Last but not least, we would like to thank the three reviewers — M. Haney and two anonymous reviewers, the assistant editor L. Valentina Socco, and the associate editor M. Asten for their constructive reviews and comments.

REFERENCES

Choose Top of pageAbstractINTRODUCTIONBACKGROUNDMETHODSSYNTHETIC TESTSFIELD DATA INVERSIONDISCUSSIONCONCLUSIONACKNOWLEDGMENTSREFERENCES <<APPENDIX APARAMETER SETTI...APPENDIX BEMPIRICAL EQUAT...CITING ARTICLES

1. Akimov, A. T., 1973, Logging in shallow dry boreholes for studying geotechnical and geodynamic characteristics of frozen soils: in Sanger, F. J., and P. J.. Hyde, eds., *Proceedings of International Conference on Permafrost, U.S.S.R. Contribution*, U.S. National Academy of Sciences, 452–456. Open URL [Google Scholar]

2. Barnes, D. F., 1963, A review of geophysical methods for delineating permafrost: in Woods, K. B., ed., *Proceedings of International Conference on Permafrost*, U.S. National Academy of Sciences, 349–355. Open URL [Google Scholar]

3. Beaty, K. S., D. R. Schmitt, and M. Sacchi, 2002, Simulated annealing inversion of multimode Rayleigh wave dispersion curves for geological structure: *Geophysical Journal International*, **151**, 622–631, doi:https://doi.org/10.1046/j.1365-246X.2002.01809.x. [Crossref] [Web of Science] Open URL [Google Scholar]

4. Bergamo, P., C. Comina, S. Foti, and M. Maraschini, 2011, Seismic characterization of shallow bedrock sites with multimodal Monte Carlo inversion of surface wave data: *Soil Dynamics and Earthquake Engineering*,**31**, 530–534, doi: https://doi.org/10.1016/j.soildyn.2010.10.006. [Crossref] [Web of Science] Open URL [Google Scholar]

5. Black, R. F., 1964, Gubik formation of quaternary age in northern Alaska: Exploration of naval petroleum reserve no. 4 and adjacent areas, Northern Alaska, 1944–53: U.S. Geological Survey, Professional paper, 59–91. Open URL [Google Scholar]

6. Boiero, D., E. Wiarda, and P. Vermeer, 2013, Surface- and guided-wave inversion for near-surface modeling in land and shallow marine seismic data: *The Leading Edge*, **32**, 638–646, doi:https://doi.org/10.1190/tle32060638.1. [Abstract] Open URL [Google Scholar]

7. Brown, J., 1969, Ionic concentration gradient in permafrost, Barrow, Alaska: U.S. Army Cold Regions Research and Engineering Laboratory, Research report. Open URL [Google Scholar]

8. Collins, F. R., and M. C. Brewer, 1961, Core tests and test wells, Barrow area, Alaska: Exploration of naval petroleum reserve no. 4 and adjacent areas, northern Alaska, 1944-53. Part 5, Subsurface geology and engineering data: U.S. Geological Survey, Professional paper, 569–644. Open URL [Google Scholar]

9. Cox, M., E. F. Scherrer, and R. Chen, 1999, *Static corrections for seismic reflection surveys*: SEG. [Abstract] Open URL [Google Scholar]

10. Douma, H., and M. Haney, 2013, Exploring nonlinearity and nonuniqueness in surface-wave inversion for near-surface velocity estimation: *The Leading Edge*, **32**, 648–655, doi:https://doi.org/10.1190/tle32060648.1. [Abstract] Open URL [Google Scholar]

11. Forbriger, T., 2003a, Inversion of shallow-seismic wavefields: I. Wavefield transformation: *Geophysical Journal International*, **153**, 719–734, doi: https://doi.org/10.1046/j.1365-246X.2003.01929.x. [Crossref] [Web of Science] Open URL [Google Scholar]

12. Forbriger, T., 2003b, Inversion of shallow-seismic wavefields: II. Inferring subsurface properties from wavefield transforms: *Geophysical Journal International*, **153**, 735–752, doi: https://doi.org/10.1046/j.1365-246X.2003.01985.x. [Crossref] [Web of Science] Open URL [Google Scholar]

13. Gautier, D. L., K. J. Bird, R. R. Charpentier, A. Grantz, D. W. Houseknecht, T. R. Klett, T. E. Moore, J. K. Pitman, C. J. Schenk, J. H. Schuenemeyer, K. Sorensen, M. E. Tennyson, Z. C. Valin, and C. J. Wandrey, 2009, Assessment of undiscovered oil and gas in the Arctic: *Science*, **324**, 1175–1179, doi:https://doi.org/10.1126/science.1169467. [Crossref] [Web of Science] Open URL [Google Scholar]

14. Gilichinsky, D., E. Rivkina, C. Bakermans, V. Shcherbakova, L. Petrovskaya, S. Ozerskaya, N. Ivanushkina, G. Kochkina, K. Laurinavichuis, S. Pecheritsina, R. Fattakhova, and J. M. Tiedje, 2005, Biodiversity of cryopegs in permafrost: *FEMS Microbiology Ecology*, **53**, 117–128, doi:https://doi.org/10.1016/j.femsec.2005.02.003. [Crossref] [Web of Science] Open URL [Google Scholar]

15. Hamilton, E. L., 1976, Attenuation of shear waves in marine sediments: *Journal of the Acoustical Society of America*, **60**, 334–338, doi: https://doi.org/10.1121/1.381111. [Crossref] [Web of Science] Open URL [Google Scholar]

16. Harvey, D. J., 1981, Seismogram synthesis using normal mode superposition: The locked mode approximation: *Geophysical Journal of the Royal Astronomical Society*, **66**, 37–69, doi:https://doi.org/10.1111/j.1365-246X.1981.tb05947.x. [Crossref] [Web of Science] Open URL [Google Scholar]

17. Hauck, C., and C. Kneisel, 2008, *Applied geophysics in periglacial environments*: Cambridge University Press. [Crossref] Open URL [Google Scholar]

18. Hayashi, K., 2012, Analysis of surface-wave data including higher modes using the genetic algorithm, GeoCongress 2012: American Society of Civil Engineers, 2776–2785. Open URL [Google Scholar]

19. Herrmann, R. B., 2004, Computer programs in seismology, version 3.30, http://www.eas.slu.edu/eqc/eqccps.html, accessed 15 January 2012. Open URL [Google Scholar]

20. Hilbich, C., 2010, Time-lapse refraction seismic tomography for the detection of ground ice degradation: *The Cryosphere*, **4**, 243–259, doi: https://doi.org/10.5194/tc-4-243-2010. [Crossref] [Web of Science] Open URL [Google Scholar]

21. Hinkel, K. M., and F. E. Nelson, 2003, Spatial and temporal patterns of active layer thickness at Circumpolar Active Layer Monitoring (CALM) sites in northern Alaska 1995-2000: *Journal of Geophysical Research*, **108**, 8168, doi: https://doi.org/10.1029/2001JD000927. [Crossref] [Web of Science] Open URL [Google Scholar]

22. Hubbard, S. S., C. Gangodagamage, B. Dafflon, H. Wainwright, J. Peterson, A. Gusmeroli, C. Ulrich, Y. Wu, C. Wilson, J. Rowland, C. Tweedie, and S. D. Wullschleger, 2013, Quantifying and relating land-surface and subsurface variability in permafrost environments using LiDAR and surface geophysical datasets: *Hydrogeology Journal*, **21**, 149–169, doi: https://doi.org/10.1007/s10040-012-0939-y. [Crossref] [Web of Science] Open URL [Google Scholar]

23. Huyer, W., and A. Neumaier, 1999, Global optimization by multilevel coordinate search: *Journal of Global Optimization*, **14**, 331–355, doi: https://doi.org/10.1023/A:1008382309369. [Crossref] [Web of Science] Open URL [Google Scholar]

24. Ikeda, T., T. Matsuoka, T. Tsuji, and K. Hayashi, 2012, Multimode inversion with amplitude response of surface waves in the spatial autocorrelation method: *Geophysical Journal International*, **190**, 541–552, doi:https://doi.org/10.1111/j.1365-246X.2012.05496.x. [Crossref] [Web of Science] Open URL [Google Scholar]

25. Jones, A., V. Stolbovoy, C. Tarnocai, G. Broll, O. Spaargaren, and L. Montanarella, 2009, *Soil atlas of the northern circumpolar region*: European Commission. Open URL [Google Scholar]

26. Jorgenson, M. T., K. Yoshikawa, M. Kanveskiy, Y. L. Shur, V. Romanovsky, S. Marchenko, G. Grosse, J. Brown, and B. Jones, 2008, Permafrost characteristics of Alaska: Institute of Northern Engineering, University of Alaska, Fairbanks. Open URL [Google Scholar]

27. Justice, J. H., and C. Zuba, 1986, Transition zone reflections and permafrost analysis: *Geophysics*, **51**, 1075–1086, doi: https://doi.org/10.1190/1.1442163. [Abstract] [Web of Science] Open URL [Google Scholar]

28. Ke, G., H. Dong, Z. Cao, and L. Liu, 2010, Surface wave dispersion curve calculation in TIV medium: 80th Annual International Meeting, SEG, Expanded Abstracts, 1924–1928. Open URL [Google Scholar]

29. King, M. S., B. I. Pandit, J. A. Hunter, and M. Gajtani, 1982, Some seismic, electrical, and thermal properties of sub-seabottom permafrost from the Beaufort Sea, in French, H. M., ed., *Proceedings of the*

Fourth Canadian Permafrost Conference: National Research Council of Canada, 268–273. Open URL [Google Scholar]

30. Kneisel, C., C. Hauck, R. Fortier, and B. Moorman, 2008, Advances in geophysical methods for permafrost investigations: *Permafrost and Periglacial Processes*, **19**, 157–178, doi: https://doi.org/10.1002/ppp.616. [Crossref] [Web of Science] Open URL [Google Scholar]

31. Lu, L., and B. Zhang, 2006, Inversion of Rayleigh waves using a genetic algorithm in the presence of a low-velocity layer: *Acoustical Physics*, **52**, 701–712, doi: https://doi.org/10.1134/S106377100606011X. [Crossref] [Web of Science] Open URL [Google Scholar]

32. Lu, L. Y., C. H. Wang, and B. X. Zhang, 2007, Inversion of multimode Rayleigh waves in the presence of a low-velocity layer: Numerical and laboratory study: *Geophysical Journal International*, **168**, 1235–1246, doi:https://doi.org/10.1111/j.1365-246X.2006.03258.x. [Crossref] [Web of Science] Open URL [Google Scholar]

33. Maraschini, M., F. Ernst, S. Foti, and L. V. Socco, 2010, A new misfit function for multimodal inversion of surface waves: *Geophysics*, **75**, G31–G43, doi: https://doi.org/10.1190/1.3436539. [Abstract] [Web of Science] Open URL [Google Scholar]

34. Maraschini, M., and S. Foti, 2010, A Monte Carlo multimodal inversion of surface waves: *Geophysical Journal International*, **182**, 1557–1566, doi: https://doi.org/10.1111/j.1365-246X.2010.04703.x. [Crossref] [Web of Science] Open URL [Google Scholar]

35. Matsushima, J., M. Suzuki, Y. Kato, T. Nibe, and S. Rokugawa, 2008, Laboratory experiments on compressional ultrasonic wave attenuation in partially frozen brines: *Geophysics*, **73**, no. 2, N9–N18, doi:https://doi.org/10.1190/1.2827214. [Abstract] [Web of Science] Open URL [Google Scholar]

36. Matsushima, J., M. Suzuki, Y. Kato, and S. Rokugawa, 2011, Laboratory measurements of ultrasonic P-wave and S-wave attenuation in partially frozen unconsolidated sediments saturated with brine: 81st Annual International Meeting, SEG, Expanded Abstracts, 2130–2134. Open URL [Google Scholar]

37. Meyer, H., L. Schirrmeister, A. Andreev, D. Wagner, H.-W. Hubberten, K. Yoshikawa, A. Bobrov, S. Wetterich, T. Opel, E. Kandiano, and J. Brown, 2010, Late glacial and Holocene isotopic and environmental history of northern coastal Alaska — Results from a buried ice-wedge system at Barrow: *Quaternary Science Reviews*, **29**, 3720–3735, doi: https://doi.org/10.1016/j.quascirev.2010.08.005. [Crossref] [Web of Science] Open URL [Google Scholar]

38. Miller, R. D., J. A. Hunter, W. E. Doll, B. J. Carr, R. A. Burns, R. L. Good, D. R. Laflen, and M. Douma, 2000, Imaging permafrost with shallow P- and S-wave reflection: 70th Annual International Meeting, SEG, Expanded Abstracts, 1339–1342. Open URL [Google Scholar]

39. Mueller, J. L., and S. Siltanen, 2012, *Linear and nonlinear inverse problems with practical applications*: Society for Industrial and Applied Mathematics. [Crossref] Open URL [Google Scholar]

40. Nelder, J. A., and R. Mead, 1965, A simplex-method for function minimization: *Computer Journal*, **7**, 308–313, doi: https://doi.org/10.1093/comjnl/7.4.308. [Crossref] [Web of Science] Open URL [Google Scholar]

41. Neumaier, A., 2000, MCS: global optimization by Multilevel Coordinate Search, version 2.0, http://www.mat.univie.ac.at/~neum/software/mcs/, accessed 22 July 2012. Open URL [Google Scholar]
42. O'Neill, A., M. Dentith, and R. List, 2003, Full-waveform P-SV reflectivity inversion of surface waves for shallow engineering applications: *Exploration Geophysics*, **34**, 158–173, doi:https://doi.org/10.1071/EG03158. [Abstract] [Web of Science] Open URL [Google Scholar]
43. O'Neill, A., and T. Matsuoka, 2005, Dominant higher surface-wave modes and possible inversion pitfalls: *Journal of Environmental and Engineering Geophysics*, **10**, 185–201, doi:https://doi.org/10.2113/JEEG10.2.185. [Abstract] [Web of Science] Open URL [Google Scholar]
44. O'Sullivan, J., 1966, Geochemistry of permafrost, Barrow, Alaska: in Woods, K. B., et al., eds., *Proceedings of International Conference on Permafrost, National Academy of Sciences*, U. S. National Academy of Sciences, **1287**, 30–37. Open URL [Google Scholar]
45. Pan, Y., J. Xia, and C. Zeng, 2013, Verification of correctness of using real part of complex root as Rayleigh-wave phase velocity with synthetic data: *Journal of Applied Geophysics*, **88**, 94–100, doi:https://doi.org/10.1016/j.jappgeo.2012.09.012. [Crossref] [Web of Science] Open URL [Google Scholar]
46. Pandit, B. I., and M. S. King, 1979, A study of the effects of pore-water salinity on some physical properties of sedimentary rocks at permafrost temperatures: *Canadian Journal of Earth Sciences*, **16**, 1566–1580, doi:https://doi.org/10.1139/e79-143. [Crossref] [Web of Science] Open URL [Google Scholar]
47. Park, C. B., R. D. Miller, and J. H. Xia, 1999, Multichannel analysis of surface waves: *Geophysics*, **64**, 800–808, doi: https://doi.org/10.1190/1.1444590. [Abstract] [Web of Science] Open URL [Google Scholar]
48. Pavlakovic, B., M. Lowe, D. Alleyne, and P. Cawley, 1997, Disperse: A general purpose program for creating dispersion curves, in Thompson, D., and D. Chimenti, eds., *Review of progress in quantitative nondestructive evaluation*: Springer, vol. 16, 185–192. [Crossref] Open URL [Google Scholar]
49. Pošík, P., W. Huyer, and L. Pál, 2012, A comparison of global search algorithms for continuous black box optimization: *Evolutionary Computation*, **20**, 509–541, doi: https://doi.org/10.1162/EVCO_a_00084. [Crossref] [Web of Science] Open URL [Google Scholar]
50. Press, W. H., S. A. Teukolsky, W. T. Vetterling, and B. P. Flannery, 1992, *Numerical recipes in C: The art of scientific computing*: Cambridge University Press. Open URL [Google Scholar]
51. Ramachandran, K., G. Bellefleur, T. Brent, M. Riedel, and S. Dallimore, 2011, Imaging permafrost velocity structure using high resolution 3D seismic tomography: *Geophysics*, **76**, no. 5, B187–B198, doi:https://doi.org/10.1190/geo2010-0353.1. [Abstract] [Web of Science] Open URL [Google Scholar]
52. Rix, G. J., and E. A. Leipski, 1991, *Accuracy and resolution of surface wave inversion: Recent advances in instrumentation, data acquisition and testing in soil dynamics*, ASCE, 17–32. Open URL [Google Scholar]

53. Ryden, N., and M. J. S. Lowe, 2004, Guided wave propagation in three-layer pavement structures: *Journal of the Acoustical Society of America*, **116**, 2902–2913, doi: https://doi.org/10.1121/1.1808223. [Crossref] [Web of Science] Open URL [Google Scholar]

54. Ryden, N., and C. B. Park, 2004, Surface waves in inversely dispersive media: *Near Surface Geophysics*, **2**, 187–197, doi: https://doi.org/10.3997/1873-0604.2004016. [Crossref] [Web of Science] Open URL [Google Scholar]

55. Ryden, N., and C. B. Park, 2006, Fast simulated annealing inversion of surface waves on pavement using phase-velocity spectra: *Geophysics*, **71**, no. 4, R49–R58, doi: https://doi.org/10.1190/1.2204964. [Abstract] [Web of Science] Open URL [Google Scholar]

56. Sain, K., and A. K. Singh, 2011, Seismic quality factors across a bottom simulating reflector in the Makran Accretionary Prism, Arabian Sea: *Marine and Petroleum Geology*, **28**, 1838–1843, doi:https://doi.org/10.1016/j.marpetgeo.2011.03.013. [Crossref] [Web of Science] Open URL [Google Scholar]

57. Sain, K., A. K. Singh, N. K. Thakur, and R. Khanna, 2009, Seismic quality factor observations for gas-hydrate-bearing sediments on the western margin of India: *Marine Geophysical Researches*, **30**, 137–145, doi: https://doi.org/10.1007/s11001-009-9073-1. [Crossref] [Web of Science] Open URL [Google Scholar]

58. Sellmann, P. V., J. Brown, R. Lewellen, H. McKim, and C. Merry, 1975, The classification and geomorphic implications of thaw lakes on the Arctic coastal plain, Alaska: U.S. Army Cold Regions Research and Engineering Laboratory, Research report. Open URL [Google Scholar]

59. Sheriff, R. E., 2002, *Encyclopedic dictionary of applied geophysics*: SEG, 203–217. [Abstract] Open URL [Google Scholar]

60. Snieder, R., 1998, The role of nonlinearity in inverse problems: *Inverse Problems*, **14**, 387–404, doi:https://doi.org/10.1088/0266-5611/14/3/003. [Crossref] [Web of Science] Open URL [Google Scholar]

61. Socco, L. V., and D. Boiero, 2008, Improved Monte Carlo inversion of surface wave data: *Geophysical Prospecting*, **56**, 357–371, doi: https://doi.org/10.1111/j.1365-2478.2007.00678.x. [Crossref] [Web of Science] Open URL [Google Scholar]

62. Socco, L. V., S. Foti, and D. Boiero, 2010, Surface-wave analysis for building near-surface velocity models — Established approaches and new perspectives: *Geophysics*, **75**, no. 5, A83–A102, doi:https://doi.org/10.1190/1.3479491. [Abstract] [Web of Science] Open URL [Google Scholar]

63. Spetzler, H., and D. L. Anderson, 1968, The effect of temperature and partial melting on velocity and attenuation in a simple binary system: *Journal of Geophysical Research*, **73**, 6051–6060, doi:https://doi.org/10.1029/JB073i018p06051. [Crossref] [Web of Science] Open URL [Google Scholar]

64. Strobbia, C., A. Glushchenko, A. Laake, P. Vermeer, T. J. Papworth, and Y. Ji, 2009, Arctic near surface challenges: The point receiver solution to coherent noise and statics: *First Break*, **27**, 69–76. Open URL [Google Scholar]

65. Thurston, D. K., and L. A. Theiss, and U. S. M. M. S. A. O. Region, 1987, Geologic report for the Chukchi Sea planning area, Alaska: Regional geology, petroleum geology, and environmental geology: U.S.

Department of the Interior, Minerals Management Service, Alaska OCS Region. Open URL [Google Scholar]

66. Timur, A., 1968, Velocity of compressional waves in porous media at permafrost temperatures: *Geophysics*,**33**, 584–595, doi: https://doi.org/10.1190/1.1439954. [Abstract] [Web of Science] Open URL [Google Scholar]

67. Trupp, R., J. Hastings, S. Cheadle, and R. Vesely, 2009, Seismic in arctic environs: Meeting the challenge: *The Leading Edge*, **28**, 936–942, doi: https://doi.org/10.1190/1.3192840. [Abstract] Open URL [Google Scholar]

68. Tsuji, T., T. A. Johansen, B. O. Ruud, T. Ikeda, and T. Matsuoka, 2012, Surface-wave analysis for identifying unfrozen zones in subglacial sediments: *Geophysics*, **77**, no. 3, EN17–EN27, doi:https://doi.org/10.1190/geo2011-0222.1. [Abstract] [Web of Science] Open URL [Google Scholar]

69. Velli, Y. Y., and P. A. Grishin, 1983, On the functional dependence of the freezing point of soils on the composition of water soluble salts in an interstitial solution, Rheology of soils and engineering geocryology (translated from Russian): Canada Institute for Scientific and Technical Information, 193–196. Open URL [Google Scholar]

70. Wathelet, M., D. Jongmans, and M. Ohrnberger, 2004, Surface-wave inversion using a direct search algorithm and its application to ambient vibration measurements: *Near Surface Geophysics*, **2**, 211–221, doi: https://doi.org/10.3997/1873-0604.2004018. [Crossref] [Web of Science] Open URL [Google Scholar]

71. Williams, J. R., 1970, Ground water in the permafrost regions of Alaska: Ground water in permafrost regions in Alaska occurs according to the same geologic and hydrologic principles prevailing in temperate regions: U.S. Geological Survey. Open URL [Google Scholar]

72. Williams, J. R., and L. D. Carter, 1984, Engineering-geologic maps of northern Alaska, Barrow quadrangle: U.S. Geological Survey, Open-file report 84–124. Open URL [Google Scholar]

73. Xia, J. H., R. D. Miller, and C. B. Park, 1999, Estimation of near-surface shear-wave velocity by inversion of Rayleigh waves: *Geophysics*, **64**, 691–700, doi: https://doi.org/10.1190/1.1444578. [Abstract] [Web of Science] Open URL [Google Scholar]

74. Xia, J. H., R. D. Miller, C. B. Park, and G. Tian, 2003, Inversion of high frequency surface waves with fundamental and higher modes: *Journal of Applied Geophysics*, **52**, 45–57, doi:https://doi.org/10.1016/S0926-9851(02)00239-2. [Crossref] [Web of Science] Open URL [Google Scholar]

75. Yilmaz, O., and A. Kocaoglu, 2012, Effect of lateral heterogeneity in the soil column on shear-wave velocity estimation by Rayleigh-wave inversion: *The Leading Edge*, **31**, 758–765, doi:https://doi.org/10.1190/tle31070758.1. [Abstract] Open URL [Google Scholar]

76. Yoshikawa, K., V. Romanovsky, N. Duxbury, J. Brown, and A. Tsapin, 2004, The use of geophysical methods to discriminate between brine layers and freshwater taliks in permafrost regions: *Journal of Glaciology and Geocryology*, **26**, 301–309. Open URL [Google Scholar]

77. Zhang, S. X., and L. S. Chan, 2003, Possible effects of misidentified mode number on Rayleigh wave inversion: *Journal of Applied Geophysics*, **53**, 17–29, doi: https://doi.org/10.1016/S0926-9851(03)00014-4. [Crossref] [Web of Science] Open URL [Google Scholar]

78. Zimmerman, R. W., and M. S. King, 1986, The effect of the extent of freezing on seismic velocities in unconsolidated permafrost: *Geophysics*, **51**, 1285–1290, doi: https://doi.org/10.1190/1.1442181. [Abstract] [Web of Science] Open URL [Google Scholar]

79. Zimov, S. A., E. A. G. Schuur, and F. S. Chapin, 2006, Permafrost and the global carbon budget: *Science*,**312**, 1612–1613, doi: https://doi.org/10.1126/science.1128908. [Crossref] [Web of Science] Open URL [Google Scholar]

APPENDIX APARAMETER SETTINGS AND TERMINATION CRITERIA OF THE GLOBAL-LOCAL HYBRID OPTIMIZATION METHOD

Choose Top of pageAbstractINTRODUCTIONBACKGROUNDMETHODSSYNTHETIC TESTSFIELD DATA INVERSIONDISCUSSIONCONCLUSIONACKNOWLEDGMENTSREFERENCESAPPENDIX APARAMETER SETTI... <<APPENDIX BEMPIRICAL EQUAT...CITING ARTICLES

MCS is equipped with a set of default parameter values that have been well tested. Here we list several key controlling parameters that we use for minimizing the *n*-dimensional objective function:

1) the maximum number of function calls $Nf_{max}=50n^2$$Nfmax=50n2$ (default)
2) the maximum split level $s_{max}=5n+10$$smax=5n+10$ (default)
3) the maximum number of sweeps $N_{sw}=3n$$Nsw=3n$ (default)
4) the maximum number of local searches $N_{loc}=0$$Nloc=0$ (i.e., the local-search enhancement is turned off).

Termination criteria of the NM method are chosen to let the search process go through generous amount of iterations for optimal convergence. In addition, a tolerance in vector movement distance is used to stop the search, which is to avoid wasting large amounts of iterations on negligible function-value improvements:

1) the maximum number of function calls $Nf_{max}=700$$Nfmax=700$
2) the fractional tolerance in the simplex-vector distance moved in a search step $X_{tot}=1\times10^{-4}$$Xtot=1×10−4$.

APPENDIX BEMPIRICAL EQUATIO

Choose Top of pageAbstractINTRODUCTIONBACKGROUNDMETHODSSYNTHETIC TESTSFIELD DATA INVERSIONDISCUSSIONCONCLUSIONACKNOWLEDGMENTSREFERENCESAPPENDIX APARAMETER SETTI...APPENDIX BEMPIRICAL EQUAT... <<CITING ARTICLES

N FOR ESTIMATING FREEZING POINT OF SALINE SOILS

According to Velli and Grishin (1983), the freezing point of saline soils can be determined from

$$T_{fp} = -T_k(S_n 1000 + S_n), \quad Tfp = -Tk(Sn1000 + Sn),$$

where S^nSn is salinity in g/lg/l (or parts per thousand), T^kTk is a reference temperature (57°C for sea salt; 62°C for NaCl).

Cited by

Ali Shaiban, Sjoerd de Ridder, Andrew Curtis. 2018. Surface-wave inversion by wavefield reconstruction and wave-equation inversion. SEG Technical Program Expanded Abstracts, 2516-2520.
Abstract | PDF (5359 KB) | PDF w/Links (3050 KB) | Permissions

Zhaolun Liu, Jing Li, Sherif M. Hanafy, Gerard Schuster. 2018. 3D wave-equation dispersion inversion of surface waves. SEG Technical Program Expanded Abstracts, 4733-4737.
Abstract | PDF (5268 KB) | PDF w/Links (5280 KB) | Permissions

Zhaolun Liu, Lianjie Huang. 2018. Multiscale and layer-stripping wave-equation dispersion inversion of Rayleigh waves. SEG Technical Program Expanded Abstracts, 2536-2540.
Abstract | PDF (827 KB) | PDF w/Links (840 KB) | Permissions

Binbin Mi, Jianghai Xia, Chao Shen, Limin Wang. (2018) Dispersion Energy Analysis of Rayleigh and Love Waves in the Presence of Low-Velocity Layers in Near-Surface Seismic Surveys. *Surveys in Geophysics* **39**:2, 271-288. Online publication date: 31-Oct-2017.
Crossref

Zhaolun Liu, Jing Li, Gerard Schuster. 2017. 3D wave-equation dispersion inversion of surface waves. SEG Global Meeting Abstracts, 22-26.
Abstract | PDF (3592 KB) | Permissions

Yuxin Wu, Seiji Nakagawa, Timothy J. Kneafsey, Baptiste Dafflon, Susan Hubbard. (2017) Electrical and seismic response of saline permafrost soil during freeze - Thaw transition. *Journal of Applied Geophysics* **146**, 16-26. Online publication date: 1-Nov-2017.
Crossref

Jonathan Ajo-Franklin, Shan Dou, Thomas Daley, Barry Freifeld, Michelle Robertson, Craig Ulrich, Todd Wood, Ian Eckblaw, Nathan Lindsey, Eileen Martin, Anna Wagner. 2017. Time-lapse surface wave monitoring of permafrost thaw using distributed acoustic sensing and a permanent automated seismic source. SEG Technical Program Expanded Abstracts, 5223-5227.
Abstract | PDF (5041 KB) | PDF w/Links (5046 KB) | Permissions

Yao Wang, Richard Miller, Shelby Peterie, Steven Sloan, Mark Moran, Harley Cudney. 2017. Tunnel detection by full-waveform inversion at Yuma Proving Ground, Arizona. SEG Technical Program Expanded Abstracts, 2660-2665.
Abstract | PDF (1979 KB) | PDF w/Links (919 KB) | Permissions

Shan Dou, Jonathan Ajo-Franklin, Baptiste Dafflon, John Peterson, Craig Ulrich, Susan Hubbard, Douglas Dreger. 2017. Surface-wave imaging of inversely dispersive media: A permafrost example. SEG Technical Program Expanded Abstracts, 5192-5196.
Abstract | PDF (3376 KB) | PDF w/Links (3377 KB) | Permissions

Yao Wang, Richard Miller, Shelby Peterie, Steven Sloan, Mark Moran, Harley Cudney. 2017. A focusing study of near-surface full-waveform inversion based on wave-mode separation. SEG Technical Program Expanded Abstracts, 2632-2636.
Abstract | PDF (1948 KB) | PDF w/Links (917 KB) | Permissions

2017. Special Global Session and Special Session I Complete Session. SEG Technical Program Expanded Abstracts 2017, 3976-5277.
Abstract | PDF (43584 KB) | PDF w/Links (25521 KB) | Permissions

2017. Mining and Geothermal and Near Surface Complete Session. SEG Technical Program Expanded Abstracts 2017, 2425-2736.
Abstract | PDF (44890 KB) | PDF w/Links (26948 KB) | Permissions

Baptiste Dafflon, Rusen Oktem, John Peterson, Craig Ulrich, Anh Phuong Tran, Vladimir Romanovsky, Susan S. Hubbard. (2017) Coincident aboveground and belowground autonomous monitoring to quantify covariability in permafrost, soil, and vegetation properties in Arctic tundra. *Journal of Geophysical Research: Biogeosciences* **122**:6, 1321-1342.
Online publication date: 3-Jun-2017.
Crossref
Shan Dou, Seiji Nakagawa, Douglas Dreger, Jonathan Ajo-Franklin. (2017) An effective-medium model for P-wave velocities of saturated, unconsolidated saline permafrost. *GEOPHYSICS* **82**:3, EN33-EN50.
Online publication date: 21-Mar-2017.
Abstract | Full Text | PDF (2699 KB) | PDF w/Links (812 KB) | Permissions
Jing Li, Zongcai Feng, Gerard Schuster. (2017) Wave-equation dispersion inversion. *Geophysical Journal International* **208**:3, 1567-1578.
Online publication date: 10-Dec-2016.
Crossref
Shawn C. Griffiths, Brady R. Cox, Ellen M. Rathje, David P. Teague. (2016) Surface-Wave Dispersion Approach for Evaluating Statistical Models That Account for Shear-Wave Velocity Uncertainty. *Journal of Geotechnical and Geoenvironmental Engineering* **142**:11, 04016061.
Online publication date: 1-Nov-2016.
Crossref
Brady R. Cox, David P. Teague. (2016) Layering ratios: a systematic approach to the inversion of surface wave data in the absence of *a priori* information. *Geophysical Journal International* **207**:1, 422-438.
Online publication date: 1-Aug-2016.
Crossref
2016. Passive Seismic Complete Session. SEG Technical Program Expanded Abstracts 2016, 2492-2769.
Abstract | PDF (69242 KB) | PDF w/Links (31466 KB) | Permissions
Eileen Martin, Nathaniel Lindsey, Shan Dou, Jonathan Ajo-Franklin, Thomas Daley, Barry Freifeld, Michelle Robertson, Craig Ulrich, Anna Wagner, Kevin Bjella. 2016. Interferometry of a roadside DAS array in Fairbanks, AK. SEG Technical Program Expanded Abstracts 2016, 2725-2729.
Abstract | PDF (4665 KB) | PDF w/Links (2135 KB) | Permissions
Jing Li, Gerard Schuster. 2016. Skeletonized wave equation of surface wave dispersion inversion. SEG Technical Program Expanded Abstracts 2016, 3630-3635.
Abstract | PDF (3135 KB) | PDF w/Links (1264 KB) | Permissions
2016. Seismic Inversion Complete Session. SEG Technical Program Expanded Abstracts 2016, 3533-3818.
Abstract | PDF (71009 KB) | PDF w/Links (31474 KB) | Permissions
Yudi Pan, Jianghai Xia, Yixian Xu, Lingli Gao, Zongbo Xu. (2016) Love-wave waveform inversion in time domain for shallow shear-wave velocity. *GEOPHYSICS* **81**:1, R1-R14.
Online publication date: 16-Nov-2015.
Abstract | Full Text | PDF (9182 KB) | PDF w/Links (1199 KB) | Permissions
Shan Dou, Seiji Nakagawa, Douglas Dreger, Jonathan Ajo-Franklin. (2016) A rock-physics investigation of unconsolidated saline permafrost: P-wave properties from laboratory ultrasonic measurements. *GEOPHYSICS***81**:1, WA233-WA245.
Online publication date: 29-Jan-2016.
Abstract | Full Text | PDF (2468 KB) | PDF w/Links (655 KB) | Permissions
Nils Ryden. 2015. Seismic pavement testing. International Conference on Engineering Geophysics, Al Ain, United Arab Emirates, 15-18 November 2015, 14-18.
Abstract | PDF (784 KB) | Permissions
Yudi Pan*, Lingli Gao, Jianghai Xia. 2015. Full waveform inversion of Rayleigh waves for near-surface shear-wave velocity. Near-Surface Asia Pacific Conference, Waikoloa, Hawaii, 7-10 July 2015, 253-256.
Abstract | PDF (903 KB) | Permissions
Andrew Binley, Susan S. Hubbard, Johan A. Huisman, André Revil, David A. Robinson, Kamini Singha, Lee D. Slater. (2015) The emergence of hydrogeophysics for improved understanding of subsurface processes over multiple scales. *Water Resources Research* **51**:6, 3837-3866.
Online publication date: 15-Jun-2015.
Crossref
Haruko M. Wainwright, Baptiste Dafflon, Lydia J. Smith, Melanie S. Hahn, John B. Curtis, Yuxin Wu, Craig Ulrich, John E. Peterson, Margaret S. Torn, Susan S. Hubbard. (2015) Identifying multiscale zonation and assessing the relative importance of polygon geomorphology on carbon fluxes in an Arctic tundra ecosystem. *Journal of Geophysical Research: Biogeosciences* **120**:4, 788-808.
Online publication date: 30-Apr-2015.
Crossref

$$M(\mathbf{m}) = \sqrt{\frac{\sum_{i=1}^{N_f} \sum_{j=1}^{N_v} (S_{ij} - O_{ij})^2}{N_f N_v}},$$

where model parameters such as layer thicknesses and S-wave velocities are the elements of the model vector $\mathbf{m}$. M represents the RMSD that measures the overall size of the misfit between the synthetic dispersion spectrum (S) for an estimated model $\mathbf{m}$ and the observed counterpart (O), N_f is the number of sampling points along the f axis (frequency) of the dispersion spectrum, and N_v is the number of sampling points along the v axis (velocity) of the dispersion spectrum. Note that we apply a global normalization to the synthetic and the observed dispersion spectrum; that is, each dispersion spectrum is normalized by its maximum spectral amplitude. In this way, relative amplitudes of the dispersion spectra are preserved (no trace normalization is applied) so that the energy partition across the multimodal wavefield is used in the inversion. An important observation is that the evaluation of M requires a full-wavefield modeling operation (S); this step is responsible for the large computational cost of our inversion approach.

Optimization techniques: Derivative-free global-local hybrid method

The inversion procedure can be posed as a bound-constrained optimization problem, for which we seek the optim model $\mathbf{m}$ that minimizes the multivariable objective function $M(\mathbf{m})$:

$$\begin{aligned} &\text{minimize} && M(\mathbf{m}); && [\mathbf{m}]_n = \{m_i\} \\ &\text{subject to} && m_i^{(l)} \le m_i \le m_i^{(u)}, && i = 1, 2, \ldots, n \end{aligned},$$